SANDIA REPORT
SAND2008-7608
Unlimited Release
Printed November 2008

LDRD Final Report on Theory and Exploration of Quantum-Dot Optical Nonlinearities and Coherences

Weng W. Chow

Prepared by
Sandia National Laboratories
Albuquerque, New Mexico 87185 and Livermore, California 94550

Sandia is a multiprogram laboratory operated by Sandia Corporation,
a Lockheed Martin Company, for the United States Department of Energy's
National Nuclear Security Administration under Contract DE-AC04-94AL85000.

Issued by Sandia National Laboratories, operated for the United States Department of Energy by Sandia Corporation.

Available to DOE and DOE contractors from
U.S. Department of Energy
Office of Scientific and Technical Information
P.O. Box 62
Oak Ridge, TN 37831

Telephone: (865) 576-8401
Facsimile: (865) 576-5728
E-Mail: reports@adonis.osti.gov
Online ordering: http://www.osti.gov/bridge

Available to the public from
U.S. Department of Commerce
National Technical Information Service
5285 Port Royal Rd.
Springfield, VA 22161

Telephone: (800) 553-6847
Facsimile: (703) 605-6900
E-Mail: orders@ntis.fedworld.gov
Online order: http://www.ntis.gov/help/ordermethods.asp?loc=7-4-0#online

SAND2008-7608
Unlimited Release
Printed November 2008

LDRD Final Report on Theory and Exploration of Quantum-dot Optical Nonlinearities and Coherences

Weng Chow
Semiconductor Materials and Device Sciences Department

Sandia National Laboratories
P. O. Box 5800
Albuquerque, NM 87185-1086

Abstract

A microscopic theory for investigating quantum-dot optical properties was developed. The theory incorporated advances on various aspects of quantum-dot physics developed at Sandia and elsewhere. Important components are a non-Markovian treatment of polarization dephasing due to carrier-carrier scattering (developed at Sandia) and a nonperturbative treatment within a polaron picture of the scattering of carriers by longitudinal-optical phonons (developed at Bremen University). A computer code was also developed that provides a detailed accounting of electronic structure influences and a consistent treatment of many-body effects, the latter via the incorporation of results from the microscopic theory. This code was used to explore quantum coherence physics in a quantum-dot system. The investigation furthers the understanding of the underlying differences between atomic quantum coherence and semiconductor quantum coherence, and helps improve the potential of using quantum coherences in quantum computing, coherent control and high-resolution spectroscopy.

Table of Contents

I. Introduction

Quantum dots (QDs) are considered key elements for the next generation of optoelectronic devices. Sandia has many QD device development projects, and the number will definitely grow in the future, as new applications emerge. To fully tap the advantages of QD technology, it is crucial to understand the underlying physics and be able to accurately predict physical behaviors over a broad range of experimental conditions.

Until recently, theoretical investigations were hindered by the lack of a comprehensive microscopic theory, because of serious complexities in QD physics. As a result, no single group could perform a complete calculation. On the other hand, several groups have made theoretical advances that contributed to solutions of various aspects of the problem. At Sandia, we developed a non-Markovian treatment of polarization dephasing due to carrier-carrier scattering within a coupled quantum-dot-quantum-well (QD-QW) system. [1] At Bremen University, a nonperturbative treatment within a polaron picture of the scattering of carriers by longitudinal-optical phonons (carrier-LO-phonon scattering) was recently completed. [2] A theory group at the Walter-Schottky Institute has developed a computer code for calculating QD electronic structures and has made it available to the public. [3] These pieces of solutions made possible the development of a comprehensive microscopic theory for QD optical response.

This LDRD project was for performing such a task at Sandia. Also proposed was the application of the theory and resulting computer code to investigate QD quantum-optical phenomena, with the goal of potential applications in quantum computing, coherent control and high-resolution spectroscopy. A by-product of this exercise was the demonstration of the analytical capability developed in this LDRD project to explore high-risk, high-payoff ideas, and put them on firm scientific foundations before undertaking the greater commitment of doing experiments.

This report highlights the results of this LDRD project and explains the physics and calculations at a level understandable to the non specialist. Details of results are published and a copy of each paper may be found at the end to this report.

II. Theory

Central to Sandia's contribution to QD theory is the realization that under high-excitation conditions (such as found in a laser) the coupling between QD and QW (wetting layer) states plays an important role in determining optical response. [4] It is therefore necessary to treat QD and QW contributions on equal footing. This is accomplished by starting with a many-body Hamiltonian of the combined QD-QW system, and working in the Hiesenberg Picture, derive the coupled equations of motion for the QD and QW polarizations. The equations have the common form:

$$\frac{dp_{\alpha\beta}}{dt} = i\omega_{\alpha\beta}p_{\alpha\beta} - i\Omega_{\alpha\beta}\left(n_\alpha + n_\beta - 1\right) + S_{\alpha\beta}^{c-p} + S_{\alpha\beta}^{c-c}$$

where α and β (discrete for QD and continuous for QW) label the states involved in the optical transition. On the right-hand side, the first term describes oscillation at the renormalized transition frequency $\omega_{\alpha\beta}$ and the second term is from absorption and stimulated emission involving the populations n_{α}, n_{β} and the laser field in the form of the renormalized Rabi frequency $\Omega_{\alpha\beta}$. Also on the right-hand side, the 3rd and 4th terms account for dephasing from carrier-phonon and carrier-carrier scattering, respectively. Details of the various contributions appearing in the above equation may be found in several publications. [1,2,4-7].

From semiclassical laser theory, the optical gain (or negative absorption) is given by [8]

$$G(\omega) = -\frac{\omega}{\varepsilon_0 ncVE(\omega)} Im\left[\sum_{\alpha\beta} \mu_{\alpha\beta} p_{\alpha\beta}\right]$$

where $_0$ and c are the permittivity and speed of light in vacuum, $\mu_{\alpha\beta}$ is the dipole matrix element, n is the background refractive index, E(ω) is the laser electric field amplitude and ω is its frequency. The active region contains the QDs, wetting layer and QW embedding the QDs, and has volume, V.

A gain or absorption calculation involves solving for the steady-state solutions to the polarization equations for given carrier density (which then defines n_{α}, n_{β} assuming quasiequilibrium condition) and weak laser probe field, E. The solution is then substituted into to the 2nd equation to obtain the gain or absorption.

III. Gain and Absorption spectra

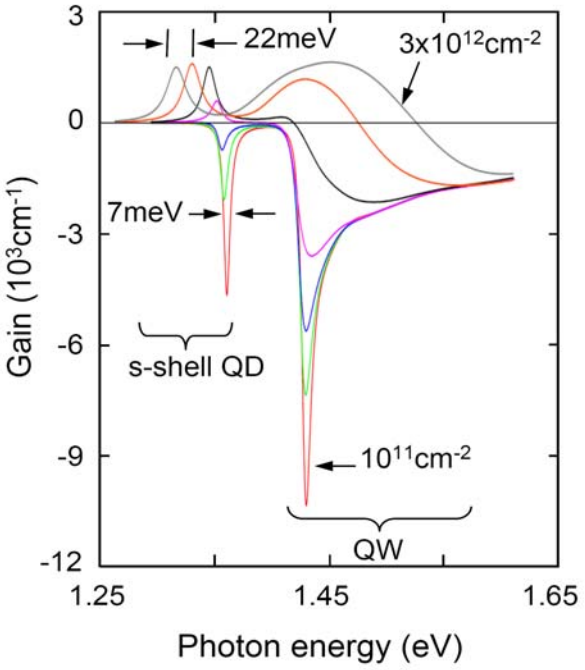

Fig. 1. Spectra showing intrinsic gain and absorption for InGaAs quantum-dot structure for increasing carrier density from 10^{11} to $3x10^{12}cm^{-2}$.

Figure 1 shows gain spectra computed using the procedure outlined in Sec. II. The curves are for T=300K and different carrier densities. The active region is a 4nm thick GaAs QW containing a density of $5x10^{10}cm^{-2}$ $In_{0.3}Ga_{0.7}As$ QDs. For the electronic structure calculations, the QD shape is approximated by a 2nm thick disk with an 18nm diameter. Each spectrum shows a QD resonance and a broad QW contribution. These spectra reveal interesting intrinsic QD properties. One is a carrier-density dependent energy shift in the QD resonances. (Note that such a shift is absent in the QW exciton resonance.) There is also appreciable spectral broadening of QD resonances with increasing carrier density, suggesting strong excitation dependence in the dephasing. [1, 6, 7] Both behaviors were observed in low excitation single-dot experiments. [9] In measurements involving an ensemble of QDs, they are likely masked by inhomogeneous broadening due to QD size and composition variations.

IV. Peak Gain Properties

Many useful laser properties are determined by the excitation dependence of peak gain. The solid curve in Fig. 2 shows the intrinsic behavior of peak gain for changing carrier density. The curve is extracted from $In_{0.3}Ga_{0.7}As$ QD gain spectra. With increasing carrier density, there is a strong initial rise in peak gain that is followed by significant gain saturation, where surprisingly, we find the QD peak gain to actually decrease with increasing carrier density. Eventually, the QW gain takes over and a positive dG_{pk}/dN is restored.

The intrinsic $dG_{pk}/dN<0$ behavior is counterintuitive and is caused by the detrimental (to having a good laser) effect of dephasing overtaking the desired effect of state-filling. [6] Fortunately, this anomaly appears to be unique to the QD-QW system and has yet to be encountered in other laser systems, whether atomic or semiconductor

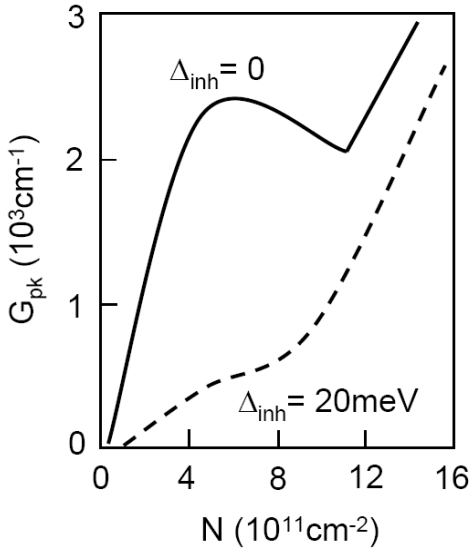

Fig. 2. Peak gain versus carrier density for intrinsic $In_{0.3}Ga_{0.7}As$ QD structure (solid curve) and with 20meV inhomogeneous broadening (dashed curve).

A good question is why $dG_{pk}/dN<0$ has to date not been observed in experiment. A reason is that with present QD samples, peak gain is reduced by inhomogeneous broadening. Because the amount of reduction is inversely proportional to the width of the QD resonance, and therefore, also inversely proportion to carrier density, one ends up with only a flattening of G_{pk} vs. N, as illustrated by the dashed curve in Fig. 2, when a sufficiently large inhomogeneous broadening is added to the intrinsic result. The $_{inh}$=20meV needed to produce the dashed curve is typical of the best presently grown QD samples and it produces a result that resembles what is typically observed in experiment. Until now, peak gain saturation in a QD system is only attributed to Pauli blocking. The microscopic theory shows that there is a second contribution from the abrupt increase in dephasing because of additional scattering channels arising from the population of QW.

Information on G_{pk} versus N is useful for many semiconductor laser simulations. To facilitate the use of our results in laser models, we introduce the following fitting function for QD peak gain:

$$G_{\mathrm{pk}}(N) = A\,\ln(N/N_0) + B\exp(-N/N_1)$$

where the first term is similar to the widely used QW gain fit function and a second term is added to account for the stronger saturation and possible gain reduction. Table 1 lists the coefficients obtained from a least-squares fit of G_{pk} versus N curves computed with the microscopic theory. These coefficients take into account the complicated dependences of scattering effects on carrier density and transition, as determined by the rigorous calculations. A more extensive discussion including information on fitting coefficients for other QD structures, in addition to fitting functions and coefficients for the carrier-induced refractive index may be found in the literature. [7]

Table I. Coefficients for $In_{0.3}Ga_{0.7}As$ QD gain fitting functions

Δ_{inh} (meV)	A (10^3/cm)	N_0 (10^{12}/cm^2)	B (10^3/cm)	N_1 (10^{12}/cm^2)
0	8.10	3.06	26.24	1.18
4	2.95	3.36	9.61	1.58
8	1.63	3.39	5.24	1.83

V. Polarization Dephasing

QD gain properties are strongly governed by polarization dephasing. Polarization decay in semiconductor (bulk, QW and QD) is nonexponential because of nondiagonal contributions to the scattering terms in the polarization equations of motion. [8] Consequently, it is only possible to speak of an effective dephasing rate that is obtained from fitting gain or absorption spectra. In the case of the QD, the dephasing rate is obtained by fitting the computed intrinsic QD resonance with a Lorentzian function,

using the Lorentzian full width at half height (FWHH) as a fitting parameter. In most cases, we are able to achieve reasonably good fits, except for the asymmetry in the actual resonance and deviations at the spectral tails. [1] Figure 3 summarizes the results by plotting the FWHH obtained from the spectral fits as a function of carrier density.

The curves illustrate the complicated nature of dephasing. First of all, the dephasing can be quite sensitive to carrier density. In addition, dephasing also depends on QD structure, and in the case of structures with multiple QD transitions, varies with resonances. To illustrate both points, we use in addition to the $In_{0.3}Ga_{0.7}As$ QD structure, an InAs QD structure. Henceforth, we refer to the InAs QD as deep QD, because its confinement potential is noticeably deeper relative to that of an $In_{0.3}Ga_{0.7}As$ QD. The deep QD emission wavelength is around 1.5μm, which makes it interesting for telecommunication applications. With the InAs deep QD, there are two resonances (s-shell and p-shell) and the effective dephasing rate for the two resonances are distinctly different in magnitude and in carrier-density dependence, as shown in Fig. 3. There is also little overlap between InAs and $In_{0.3}Ga_{0.7}As$ QD curves. The complex dephasing behaviors are obtainable only with a rigorous treatment of scattering effects. Predictions of dephasing widths or times (right axis) are consistent with experiment. [10]

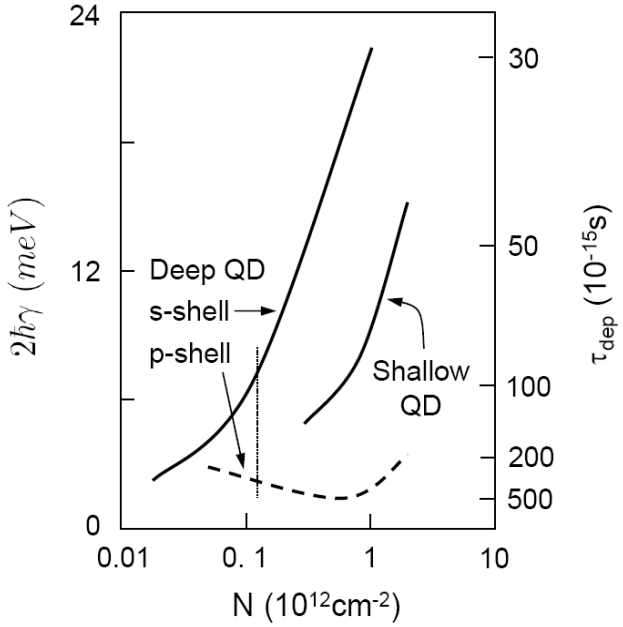

FIG. 3. Intrinsic (homogeneous) width of QD resonance (left axis) and effective dephasing lifetime (right axis) vs. carrier density. The dotted line indicates the carrier density where the InAs QD gain peak moves from the s- to p-shell resonance.

VI. Alpha Factor

The microscopic theory also gives the linewidth enhancement [11] or antiguiding [12] factor

$$\alpha = R = -2\frac{d\left(\delta n\right)/dN}{dG/dN}$$

where K is the laser field wave number and

$$\delta n(\omega) = -\frac{\omega}{K\varepsilon_0 ncVE(\omega)} \mathrm{Re}\left[\sum_{\alpha\beta} \mu_{\alpha\beta} p_{\alpha\beta}\right]$$

is the carrier-induced refractive index change. The magnitude of α provides indication of the contribution of the active medium to laser linewidth, frequency chirp and output beam quality.

Figure 4 shows the dependence of at the gain peak (where a laser typically operates) as a function of peak gain for $In_{0.3}Ga_{0.7}As$ and InAs QDs. In the range of small peak gain the curves indicate small values for the magnitude of as expected for atomic-like systems. In contrast to the bulk and QW cases, α at the gain peak can be negative.

A negative α is very desirable for high-power single-mode operation. With $\alpha>0$, filamentation (or self-focusing) limits output intensity in single-mode lasers. With $\alpha<0$, antiguiding occurs instead, and single-mode intensity is only limited by extrinsic factors such as thermal lensing.

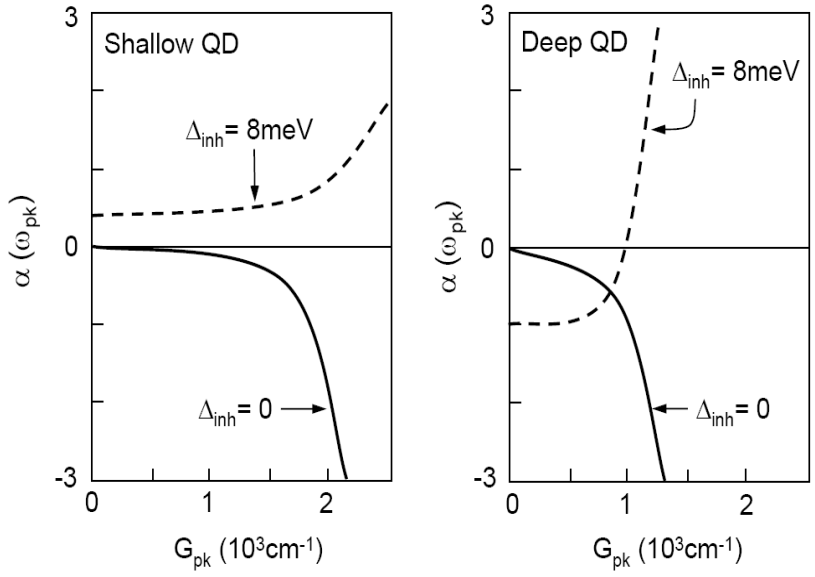

Fig. 4. α at gain peak vs. peak gain for shallow (left) and deep (right) QDs, showing both intrinsic (solid curves) and inhomogeneously-broadened behaviors (dashed curves). Only the ground state (s-shell) resonance is considered. Note that for the deep QD, $\alpha(\omega_p)$ remains negative for low excitations and with inhomogeneous broadening.

However, we note that negative α with s-shell lasing is only achievable with sufficiently small inhomogeneous broadening in the sample. The widening of δn spectrum with inhomogeneous broadening leads to a changing of the sign of α as depicted in Fig. 4. However, it was shown, theoretically and experimentally, that antiguiding at high excitation is still possible with experimentally realizable QD samples with the proper choice of QD confinement and lasing transition. [13,14]

VII. Quantum Coherences

Research on quantum coherence effects in atomic systems has stirred interest in possible optoelectronic applications. To realize this goal, we investigated in this LDRD project the physics and device engineering issues in the context of a condense-matter system. The advantages of using quantum dots (QDs) in quantum coherences include the possibility of long dephasing times and the preservation of atomic-like properties (e.g., discrete energy levels) at high temperatures. [15]

Our investigation uncovered an important difference between many-body theory (such as ours) and free-carrier treatments (adapted from atomic physics). To illustrate this difference, we present results for the slow-down factor

$$S = n_b \left(1 + \omega_p d\chi_r / d\omega_p\right)$$

where n_b is the background refractive index, ω_p is the probe frequency and χ_r is the real part of the quantum-dot susceptibility. The slow-down factor, which is a measure of the refractive index changes resulting in optical group-velocity reduction, is of interest for applications such as optical storage.

Figure 5 shows predictions of the maximum value for S as a function of pump intensity for lattice temperatures, T_L=75K. Comparison of solid and dashed curves shows an appreciable difference between many-body and free-carrier predictions. Most important of these differences is the over two orders of magnitude overestimation of the necessary pump-pulse intensity when many-body effects are neglected. Also, while both treatments predict basically the same maximum achievable S, the drive intensities for reaching saturation are drastically different. Detailed analysis reveals that the Coulomb enhancement is the primary cause for these differences. [16]

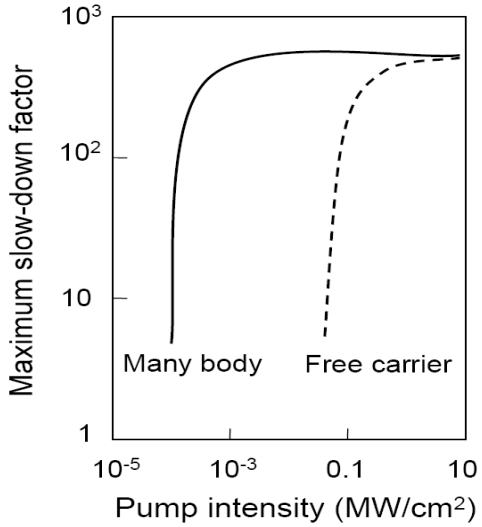

Fig. 5. Maximum slow-down factor vs. pump-pulse peak intensity for T=75K. Comparison of solid and dashed curves shows over 2 orders of magnitude difference in many-body and free-carrier predictions for the pump intensity necessary for the onset of group-velocity slowdown.

VIII. Conclusion

This 2-year LDRD project led to the development of a theory and accompanying computer codes for investigating optical properties in quantum-dot systems. In developing the theory, we used a first-principles approach that included a detailed account of the electronic structure of the coupled quantum-dot and quantum-well system; a description of light-matter interaction that allowed treatment of optical nonlinearities, ultrafast excitation and quantum coherences; and a rigorous treatment of scattering effects at the level of quantum kinetic theory. The detailed treatment of many-body effects allows the elimination of almost all free (fitting) input parameters, resulting in significant improvement in predictive capability. The code is presently providing the most advance theoretical support for in-house experiments and idea developments. For example, during the final year of the project, the theory and code were used to explore quantum-optical phenomena in quantum-dot systems. The motivation is potential applications in quantum computing, coherent control and high-resolution spectroscopy. The exercise demonstrated our capability to explore a high-risk, high-payoff idea and put it on a firm scientific foundation before undertaking the greater commitment of doing experiment.

In addition to providing state-of-the-art analytical support to Sandia's many quantum-dot research projects, the investigations also motivated new ideas relevant to Sandia initiatives in solid-state lighting, solar photovoltaic conversion and negative refraction. These ideas contributed to three LDRD new-start projects. The results of our LDRD project also provided technical supporting material in three recent BES proposals. Lastly, external recognition is evident from the 5 invited talks and 4 refereed papers.

Acknowledgements

The author wishes to thank F. Jahnke, M. Lorke, H. C. Schneider, Stephan Michael and S. W. Koch for fruitful collaborations. Support through the Senior Science Award from the Alexander von Humboldt Foundation is gratefully acknowledged. Sandia is a multiprogram laboratory operated by Sandia Corporation, a Lockheed Martin Company, for the United States Department of Energy's National Nuclear Security Administration under Contract DE-AC04-94AL85000.

References

[1] H. C. Schneider, W. W. Chow, and S. W. Koch, Phys. Rev. B 70, 235308 (2004).

[2] J. Seebeck, T.R. Nielsen, P. Gartner, and F. Jahnke, Phys. Rev. B **71**, 125327 (2005).

[3] NEXTNANO^3 device simulator, http://www.wsi.tum.de/ nextnano

[4] H.C. Schneider, W.W. Chow, and S.W. Koch, Phys. Rev. B **64**, 115315 (2001).

[5] M. Lorke, T.R. Nielsen, J. Seebeck, P. Gartner, and F. Jahnke, Phys. Rev. B **73**, 085324 (2006).

[6] M. Lorke, W. W. Chow, T.R. Nielsen, J. Seebeck, P. Gartner, and F. Jahnke, Phys. Rev. B **74**, 035334 (2006).

[7] M. Lorke, F. Jahnke and W. W. Chow Appl. Phys. Lett. **90**, 051112 (2007).

[8] W. W. Chow and S. W. Koch, Semiconductor-Laser Fundamentals: Physics of the Gain Materials (Springer, Berlin, 1999).

[9] K. Matsuda, K. Ikeda, T. Saiki, H. Saito and K. Nishi, Appl. Phys. Lett. **83**, 2250 (2003).

[10] P. Borri, W. Langbein, S. Schneider, U. Woggon, R. L. Sellin, D. Ouyang, and D. Bimberg, IEEE J. Sel. Top. Quantum Electron. **8**, 984 (2002).

[11] C.H Henry, IEEE J. Quantum Electron. **18**, 259 (1982)

[12] P. Kirkby, A. Goodwin, G. Thompson and P. Selway, IEEE J. Quantum Electron. QE-**13**, 705 (1977)

[13] H.C. Schneider, W.W. Chow and S.W. Koch, Phys. Rev. B **66**, 041310 Rapid Communication (2002).

[14] P. M. Smowton, E. J. Pearce, H. C. Schneider, W. W. Chow, M. Hopkinson, Appl. Phys. Lett. **81**, 3251 (2002).

[15] W. W. Chow, H. C. Schneider and M. C. Phillips, 'Theory of quantum coherence phenomena in semiconductor quantum dots.' Phys. Rev. A . Rev. A **68**, 053802 (2003).

[16] S. Michael, W. W. Chow, H. C. Schneider, 'Coulomb corrections to the slowdown factor in quantum-dot quantum coherence,' Appl. Phys. Lett. **89**, 181114 (2006).

Appendix I: Equations for quantum-dot microscopic theory

In this appendix, the equations derived for the quantum-dot/quantum-well system are listed. These equations are used in the code development.

Material gain

$$G = -2\frac{\nu}{\varepsilon_0 nc}\frac{2}{V}\frac{1}{E}Im\left[N_d A\mu_\alpha p_\alpha + \sum_{\mathbf{k}}\mu_k p_k\right] \tag{1}$$

Quantum dot polarization

Equation of motion

$$\begin{aligned}\frac{dp_s}{dt} &= i\left(\omega-\omega_s\right)p_s - i\Omega_s\left(n_{se}+n_{sh}-1\right)\\ &\quad -\Gamma_{ss}^{ph}p_s - \sum_{\mathbf{k}}\Gamma_{sk}^{ph}p_k - \Lambda_{ss}p_s + \sum_{\mathbf{k}}\Lambda_{sk}p_k\end{aligned} \tag{2}$$

Renormalized transition energy

$$\hbar\omega_s = \varepsilon_{se}+\varepsilon_{sh} - \sum_{\mathbf{k}}V_{s,k}\left(n_{ke}+n_{kh}\right) \tag{3}$$

Renormalized Rabi energy

$$\hbar\Omega_s = 2\wp_d E + \sum_{\mathbf{k}}V_{s,k}p_k \tag{4}$$

Coefficients for carrier-carrier scattering

$$\begin{aligned}\Lambda_{ss} &= \frac{2}{\hbar}\sum_{\mathbf{k}'}\sum_{\mathbf{q}}\sum_{\sigma}\sum_{\sigma'}\sum_{\mathbf{k}}\xi_{sk}\left[{W_q}^2 - \frac{\delta_{\sigma,\sigma'}}{2}W_q W_{|\mathbf{k}'-\mathbf{q}-\mathbf{k}|}\right]\frac{1}{\Delta-i\delta\varepsilon}\\ &\quad\times\left[n_{|\mathbf{k}'-\mathbf{q}|\sigma'}\left(1-n_{k'\sigma'}\right)\left(1-n_{k\sigma}\right)+\left(1-n_{|\mathbf{k}'-\mathbf{q}|\sigma'}\right)n_{k'\sigma'}n_{k\sigma}\right]\end{aligned} \tag{5}$$

$$\begin{aligned}\Lambda_{sk} &= \frac{2}{\hbar}\sum_{\mathbf{q}}\sum_{\sigma}\sum_{\sigma'}\sum_{\mathbf{k}'}\xi_{sk}\left[{W_q}^2 - \frac{\delta_{\sigma,\sigma'}}{2}W_q W_{|\mathbf{k}'-\mathbf{q}-\mathbf{k}|}\right]\frac{1}{\Delta+i\delta\varepsilon}\\ &\quad\times\left[n_{s\sigma}n_{|\mathbf{k}'-\mathbf{q}|\sigma'}\left(1-n_{k'\sigma'}\right)+\left(1-n_{s\sigma}\right)\left(1-n_{|\mathbf{k}'-\mathbf{q}|\sigma'}\right)n_{k'\sigma'}\right]\end{aligned} \tag{6}$$

where

$$\xi_{sk} = \frac{4\pi}{A\beta^2 N_k}\left[e^{-|\mathbf{k}-\mathbf{q}|^2/(2\beta^2)} - \left(1-\frac{kq}{\beta^2}\right)e^{-\left(k^2+\frac{q^2}{2}\right)/(2\beta^2)}\right]^2 \tag{7}$$

$$\frac{1}{N_k} = \left[1-\frac{4\pi N_d}{\beta^2}\left(\frac{h_d}{h}\right)^2\left(1+\frac{2k^2}{\beta^2}\right)e^{-k^2/\beta^2}\right] \tag{8}$$

Coefficients for carrier-phonon scattering

$$\begin{aligned}\Gamma_{ss}^{ph} &= \int_0^\infty dt' \sum_{\mathbf{k}} \left|\frac{M_{sk}}{\hbar}\right|^2 \sum_{\sigma=e,h} G_{k_\sigma}(t')\, G_{s_\sigma}(t')\, e^{i(\varepsilon_{s\sigma}-\varepsilon_{k\sigma})t'/\hbar} \\ &\quad \left\{(1-n_{k\sigma})\,\left[n_{LO}e^{i\omega_{LO}t'}+(n_{LO}+1)\,e^{-i\omega_{LO}t'}\right]+n_{k\sigma}\left[(n_{LO}+1)\,e^{i\omega_{LO}t'}+n_{LO}e^{-i\omega_{LO}t'}\right]\right\}\end{aligned} \tag{9}$$

$$\begin{aligned}\Gamma_{sk}^{ph} &= \int_0^\infty dt' A \left|\frac{M_{sk}}{\hbar}\right|^2 \sum_{\sigma=e,h} G_{k_\sigma}(t')\, G_{s_\sigma}(t')\, e^{i(\varepsilon_{k\sigma}-\varepsilon_{s\sigma})t'/\hbar} \\ &\quad \left\{(1-n_{s\sigma})\,\left[n_{LO}e^{i\omega_{LO}t'}+(n_{LO}+1)\,e^{-i\omega_{LO}t'}\right]+n_{s\sigma}\left[(n_{LO}+1)\,e^{i\omega_{LO}t'}+n_{LO}e^{-i\omega_{LO}t'}\right]\right\}\end{aligned} \tag{10}$$

where the equation of motion for the polaron Green's function is

$$\begin{aligned}\frac{dG_{\alpha_\sigma}(t)}{dt} &= -\int_0^t dt' \,\left[(n_{LO}+1)\,e^{-i\omega_{LO}t'}+n_{LO}e^{i\omega_{LO}t'}\right]\, G_{\alpha_\sigma}(t-t') \\ &\quad \sum_{\beta_\sigma} \frac{\left|M_{\alpha_\sigma,\beta_\sigma}\right|^2}{\hbar^2} G_{\beta_\sigma}(t')\, \exp\left[i\frac{\varepsilon_{\alpha_\sigma}-\varepsilon_{\beta_\sigma}}{\hbar}t'\right]\end{aligned} \tag{11}$$

with α = s or k and σ = e or h.

<u>Quantum well</u>

Equation of motion

$$\begin{aligned}\frac{dp_k}{dt} &= +i\,(\omega-\omega_k)\,p_s - i\Omega_k\,(n_{ke}+n_{kh}-1) \\ &\quad -\Gamma_{kk}^{ph}p_k + N_d A\Gamma_{ks}^{ph}p_s + \sum_{\mathbf{k}'}\Gamma_{kk'}^{ph}p_{k'} \\ &\quad -\Lambda_{kk}p_k + N_d A\Lambda_{k,s}p_s + \sum_{\mathbf{q}}\Lambda_{k,|\mathbf{k}+\mathbf{q}|}p_{|\mathbf{k}+\mathbf{q}|}\end{aligned} \tag{12}$$

Renormalized transition energy

$$\hbar\omega_k = \varepsilon_{ke}+\varepsilon_{kh}-\sum_{\mathbf{k}'}V_{|\mathbf{k}-\mathbf{k}'|}\,(n_{k'e}+n_{k'h}) \tag{13}$$

Renormalized Rabi energy

$$\hbar\Omega_k = 2\wp_{qw}E + N_d p_s A V_{sk} + \sum_{\mathbf{k}'}V_{|\mathbf{k}-\mathbf{k}'|}p_{\mathbf{k}'} \tag{14}$$

Coefficients for carrier-carrier scattering

$$\begin{aligned}\Lambda_{kk} &= \frac{2}{\hbar}\sum_{\mathbf{q}}\sum_{\sigma}\sum_{\sigma'}\sum_{\mathbf{k}'}\left[W_q{}^2-\frac{\delta_{\sigma,\sigma'}}{2}W_q W_{|\mathbf{k}'-\mathbf{q}-\mathbf{k}|}\right]\frac{1}{\Delta-i\delta\varepsilon} \\ &\quad \left[n_{k'\sigma'}\left(1-n_{|\mathbf{k}'-\mathbf{q}|\sigma'}\right)\left(1-n_{|\mathbf{k}+\mathbf{q}|\sigma}\right)+\left(1-n_{k'\sigma'}\right)n_{|\mathbf{k}'-\mathbf{q}|\sigma'}n_{|\mathbf{k}+\mathbf{q}|\sigma}\right]\end{aligned} \tag{15}$$

$$\Lambda_{k,s} = \frac{2}{\hbar}\sum_{\sigma=e,h}\sum_{\mathbf{q}}\sum_{\mathbf{k}'}\sum_{\sigma'=e,h}\left(W_{sk}\left(q\right)^2-\frac{\delta_{\sigma,\sigma'}}{2}W_{sk}\left(q\right)W_{|\mathbf{k}'-\mathbf{q}-\mathbf{k}|}\right) \frac{1}{\Delta+i\delta\varepsilon}\left[n_{s\sigma}n_{|\mathbf{k}'-\mathbf{q}|\sigma'}\left(1-n_{k'\sigma'}\right)+\left(1-n_{s\sigma}\right)\left(1-n_{|\mathbf{k}'-\mathbf{q}|\sigma}\right)n_{k'\sigma}\right] \tag{16}$$

$$\Lambda_{k,|\mathbf{k}+\mathbf{q}|} = \frac{2}{\hbar}\sum_{\sigma=e,h}\sum_{\sigma'=e,h}\sum_{\mathbf{k}'}\left(W_q^2-\frac{\delta_{\sigma,\sigma'}}{2}W_qW_{|\mathbf{k}'-\mathbf{q}-\mathbf{k}|}\right) \frac{1}{\Delta+i\delta\varepsilon}\left[n_{k\sigma}n_{k'\sigma'}\left(1-n_{|\mathbf{k}'-\mathbf{q}|}\right)+\left(1-n_{k\sigma}\right)\left(1-n_{k'\sigma'}\right)n_{|\mathbf{k}'-\mathbf{q}|\sigma'}\right] \tag{17}$$

Coefficients for carrier-phonon scattering

$$\Gamma_{kk}^{ph} = \int_0^\infty dt'\sum_{\mathbf{k}'}\left|\frac{M_{kk'}}{\hbar}\right|^2\sum_{\sigma=e,h}G_{k'_\sigma}\left(t'\right)G_{k_\sigma}\left(t'\right)e^{i(\varepsilon_{k\sigma}-\varepsilon_{k'\sigma})t'/\hbar} \left\{\left(1-n_{k'\sigma}\right)\left[n_{LO}e^{i\omega_{LO}t'}+\left(n_{LO}+1\right)e^{-i\omega_{LO}t'}\right]+n_{k'\sigma}\left[\left(n_{LO}+1\right)e^{i\omega_{LO}t'}+n_{LO}e^{-i\omega_{LO}t'}\right]\right\} \tag{18}$$

$$\Gamma_{ks}^{ph} = \int_0^\infty dt'A\left|\frac{M_{ks}}{\hbar}\right|^2\sum_{\sigma=e,h}G_{s_\sigma}\left(t'\right)G_{k_\sigma}\left(t'\right)e^{i(\varepsilon_{s\sigma}-\varepsilon_{k\sigma})t'/\hbar} \left\{\left(1-n_{k\sigma}\right)\left[n_{LO}e^{i\omega_{LO}t'}+\left(n_{LO}+1\right)e^{-i\omega_{LO}t'}\right]+n_{k\sigma}\left[\left(n_{LO}+1\right)e^{i\omega_{LO}t'}+n_{LO}e^{-i\omega_{LO}t'}\right]\right\} \tag{19}$$

$$\Gamma_{kk'}^{ph} = \int_0^\infty dt'A\left|\frac{M_{kk'}}{\hbar}\right|^2\sum_{\sigma=e,h}G_{k'_\sigma}\left(t'\right)G_{k_\sigma}\left(t'\right)e^{i(\varepsilon_{k'\sigma}-\varepsilon_{k\sigma})t'/\hbar} \left\{\left(1-n_{k\sigma}\right)\left[n_{LO}e^{i\omega_{LO}t'}+\left(n_{LO}+1\right)e^{-i\omega_{LO}t'}\right]+n_{k\sigma}\left[\left(n_{LO}+1\right)e^{i\omega_{LO}t'}+n_{LO}e^{-i\omega_{LO}t'}\right]\right\} \tag{20}$$

where $G_{k\sigma}$ is determined by solving (11).

Equations as programmed in code

For the numerical computer code, the above equations are converted by allowing the quantum well index, k, to be continuous. The corresponding equations are given below.

$$G = -2\frac{\nu}{\varepsilon_0 nch}2\frac{1}{E}Im\left[N_d\left(ed_0\eta_d\right)p_\alpha+\frac{1}{2\pi}\int_0^\infty dk\ k\frac{2ed_0\eta_q}{1+\varepsilon_{rk}/\varepsilon_{g0}}p_k\right] \tag{1a}$$

$$\frac{dp_s}{dt} = +i\left(\omega_0-\omega_s\right)p_s-i\Omega_s\left(n_{se}+n_{sh}-1\right) -\Gamma_{ss}^{ph}p_s-\frac{1}{2\pi}\int_0^\infty dk\ k\ \Gamma_{sk}^{ph}p_k-\Lambda_{ss}p_s+\frac{1}{2\pi}\int_0^\infty dk\ k\ \Lambda_{sk}p_k \tag{2a}$$

$$\hbar\omega_s = \varepsilon_{se} + \varepsilon_{sh} - \int_0^\infty dk\ \theta_{sk}\left(n_{ke} + n_{kh}\right) \tag{3a}$$

$$\hbar\Omega_s = 2\wp E\left(\frac{\wp_d}{\wp}\right) + \frac{1}{2\pi}\int_0^\infty dk\ k\ \theta_{sk} p_k \tag{4a}$$

where

$$\theta_{sk} = \frac{e^2}{\pi\hbar\varepsilon_0 n^2\beta^2}\frac{1}{N_k}\int_0^\infty dq\int_0^{2\pi} d\phi\left[e^{-|\mathbf{k}-\mathbf{q}|^2/\beta^2} - \left(1-\frac{2kq}{\beta^2}\right)e^{-\left(k^2+\frac{q^2}{2}\right)/\beta^2}\right]^2$$

and N_k is defined in (8).

$$\begin{aligned}\Lambda_{ss} \;=\; & \frac{1}{2\pi}\frac{2}{\hbar}\frac{1}{(2\pi)^4}\left(\frac{e^2}{2\varepsilon_0 n^2}\right)^2\frac{4\pi}{\beta^2}\int_0^\infty dk'\ k'\int_0^{2\pi} d\phi'\sum_{\sigma=e,h}\sum_{\sigma'=e,h}\int_0^\infty dq\int_0^{2\pi} d\phi_q\int_0^\infty dk\ k \\ & \frac{1}{N_k}\left[e^{-|\mathbf{k}-\mathbf{q}|^2/(2\beta^2)} - \left(1-\frac{kq}{\beta^2}\right)e^{-\left(k^2+\frac{q^2}{2}\right)/(2\beta^2)}\right]^2 \\ & \left[\frac{1}{q{\varepsilon_q}^2} - \frac{\delta_{\sigma,\sigma'}}{2}\frac{1}{|\mathbf{k}'-\mathbf{q}-\mathbf{k}|\,\varepsilon_q\varepsilon_{|\mathbf{k}'-\mathbf{q}-\mathbf{k}|}}\right]\frac{1}{\Delta - i\delta\varepsilon} \\ & \left[n_{|\mathbf{k}'-\mathbf{q}|\sigma'}\left(1-n_{k'\sigma'}\right)\left(1-n_{k\sigma}\right) + \left(1-n_{|\mathbf{k}'-\mathbf{q}|\sigma'}\right)n_{k'\sigma'}n_{k\sigma}\right]\end{aligned} \tag{5a}$$

$$\begin{aligned}\Lambda_{sk} \;=\; & \frac{2}{\hbar}\frac{1}{(2\pi)^4}\left(\frac{e^2}{2\varepsilon_0 n^2}\right)^2\frac{4\pi}{\beta^2}\frac{1}{N_k}\int_0^\infty dq\left[e^{-|\mathbf{k}-\mathbf{q}|^2/(2\beta^2)} - \left(1-\frac{kq}{\beta^2}\right)e^{-\left(k^2+\frac{q^2}{2}\right)/(2\beta^2)}\right]^2 \\ & \int_0^{2\pi} d\phi_q\sum_{\sigma=e,h}\int_0^\infty dk'\ k'\int_0^{2\pi} d\phi'\sum_{\sigma'=e,h}\left[\frac{1}{q{\varepsilon_q}^2} - \frac{\delta_{\sigma,\sigma'}}{2}\frac{1}{|\mathbf{k}'-\mathbf{q}-\mathbf{k}|\,\varepsilon_q\varepsilon_{|\mathbf{k}'-\mathbf{q}-\mathbf{k}|}}\right]\frac{1}{\Delta + i\delta\varepsilon} \\ & \left[n_{s\sigma}n_{|\mathbf{k}'-\mathbf{q}|\sigma'}\left(1-n_{k'\sigma'}\right) + \left(1-n_{s\sigma}\right)\left(1-n_{|\mathbf{k}'-\mathbf{q}|\sigma}\right)n_{k'\sigma}\right]\end{aligned} \tag{6a}$$

$$\begin{aligned}\Gamma_{ss}^{ph} \;=\; & \frac{A}{2\pi}\int_0^\infty dt'\int_0^\infty dk\ k\left|\frac{M_{sk}}{\hbar}\right|^2\sum_{\sigma=e,h}G_{k_\sigma}\left(t'\right)G_{s_\sigma}\left(t'\right)e^{i(\varepsilon_{s\sigma}-\varepsilon_{k\sigma})t'/\hbar} \\ & \left\{\left(1-n_{k\sigma}\right)\left[n_{LO}e^{i\omega_{LO}t'} + \left(n_{LO}+1\right)e^{-i\omega_{LO}t'}\right] + n_{k\sigma}\left[\left(n_{LO}+1\right)e^{i\omega_{LO}t'} + n_{LO}e^{-i\omega_{LO}t'}\right]\right\}\end{aligned} \tag{7a}$$

$$\begin{aligned}\Gamma_{sk}^{ph} \;=\; & A\left|\frac{M_{sk}}{\hbar}\right|^2\int_0^\infty dt'\sum_{\sigma=e,h}G_{k_\sigma}\left(t'\right)G_{s_\sigma}\left(t'\right)e^{i(\varepsilon_{k\sigma}-\varepsilon_{s\sigma})t'/\hbar} \\ & \left\{\left(1-n_{s\sigma}\right)\left[n_{LO}e^{i\omega_{LO}t'} + \left(n_{LO}+1\right)e^{-i\omega_{LO}t'}\right] + n_{s\sigma}\left[\left(n_{LO}+1\right)e^{i\omega_{LO}t'} + n_{LO}e^{-i\omega_{LO}t'}\right]\right\}\end{aligned} \tag{8a}$$

where $G_{k\sigma}$ is determined by solving (11).

$$\begin{aligned}
\frac{dp_k}{dt} &= -2i\left(\frac{\wp E}{\hbar}\right)\left(\frac{\wp_{qw}/\wp}{1+\frac{\hbar k^2}{2m_r\varepsilon_{g0}}}\right)(n_{ke}+n_{kh}-1)+i\left(\Delta_0-\frac{\hbar^2k^2}{2m_r}\right)p_k \\
&\quad -i\left(n_{ke}+n_{kh}-1\right)\left[N_d\theta_{sk}p_s+\frac{1}{2\pi}\int_0^\infty dk'\ k'\ \theta_{kk'}p_{k'}\right]+ip_k\frac{1}{2\pi}\int_0^\infty dk'\ k'\ \theta_{kk'}\left(n_{k'e}+n_{k'h}\right) \\
&\quad -\Gamma^{ph}_{kk}p_k+N_dA\Gamma^{ph}_{ks}p_s+\frac{1}{2\pi}\int_0^\infty dk'\ k'\ \Gamma^{ph}_{kk'}p_{k'} \\
&\quad -\Lambda_{kk}p_k+N_d\Lambda_{ks}p_s+\int_0^\infty dq\ q\ \Lambda_{kk_f}p_{k_f}
\end{aligned} \tag{10a}$$

where

$$\theta_{kk'}=\frac{e^2}{4\pi\hbar\varepsilon_0 n^2}\int_0^{2\pi}d\phi\frac{1}{|\mathbf{k}-\mathbf{k}'|}$$

$$\begin{aligned}
\Lambda_{kk} &= \frac{2}{\hbar}\frac{1}{(2\pi)^4}\left(\frac{e^2}{2\varepsilon_0 n^2}\right)^2\int_0^\infty dq\int_0^{2\pi}d\phi\sum_{\sigma=e,h}\sum_{\sigma'=e,h}\int_0^\infty dk'\ k'\int_0^{2\pi}d\phi' \\
&\quad\times\left[\frac{1}{q\varepsilon_q^2}-\frac{\delta_{\sigma,\sigma'}}{2}\frac{1}{|\mathbf{k}'-\mathbf{q}-\mathbf{k}|\,\varepsilon_q\varepsilon_{|\mathbf{k}'-\mathbf{q}-\mathbf{k}|}}\right]\frac{1}{\Delta-i\delta\varepsilon} \\
&\quad\times\left[n_{k'\sigma'}\left(1-n_{|\mathbf{k}'-\mathbf{q}|\sigma'}\right)\left(1-n_{|\mathbf{k}+\mathbf{q}|\sigma}\right)+\left(1-n_{k'\sigma'}\right)n_{|\mathbf{k}'-\mathbf{q}|\sigma'}n_{|\mathbf{k}+\mathbf{q}|\sigma}\right]
\end{aligned} \tag{13a}$$

$$\begin{aligned}
\Lambda_{k,s} &= \frac{2}{\hbar}\frac{1}{(2\pi)^4}\left(\frac{8\pi}{\beta^2}\right)^2\left(\frac{e^2}{2\varepsilon_0 n^2}\right)^2\sum_{\sigma=e,h}\int_0^\infty dq\int_0^{2\pi}d\phi\int_0^\infty dk'k'\int_0^{2\pi}d\phi'\sum_{\sigma=e,h}\frac{1}{\Delta+i\delta\varepsilon} \\
&\quad\left[\frac{1}{q\varepsilon\left(q\right)^2}-\delta_{\sigma,\sigma'}\frac{1}{2}\frac{1}{\varepsilon\left(q\right)|\mathbf{k}'-\mathbf{q}-\mathbf{k}|\,\varepsilon\left(|\mathbf{k}'-\mathbf{q}-\mathbf{k}|\right)}\right]\left[e^{-|\mathbf{k}-\mathbf{q}|^2/\beta^2}-\left(1-\frac{2kq}{\beta^2}\right)e^{-\left(k^2+\frac{q^2}{2}\right)/\beta^2}\right] \\
&\quad\left[1-\frac{8\pi N_d}{\beta^2}\left(\frac{h_d}{h}\right)^2\left(1+\frac{4k^2}{\beta^2}\right)e^{-2k^2/\beta^2}\right]^{-2} \\
&\quad\left[n_{s\sigma}n_{|\mathbf{k}'-\mathbf{q}|\sigma'}\left(1-n_{k'\sigma'}\right)+\left(1-n_{s\sigma}\right)\left(1-n_{|\mathbf{k}'-\mathbf{q}|\sigma}\right)n_{k'\sigma}\right]
\end{aligned} \tag{14a}$$

$$q\,\Lambda_{k|\mathbf{k}+\mathbf{q}|} = \int_0^\infty dq\ \frac{2}{\hbar}\frac{1}{(2\pi)^4}\left(\frac{e^2}{2\varepsilon_0 n^2}\right)^2 \int_0^{2\pi} d\phi_q \sum_{\sigma=e,h}\int_0^\infty dk' k' \int_0^{2\pi} d\phi' \times\left[\frac{1}{q\varepsilon_q^2} - \frac{\delta_{\sigma,\sigma'}}{2}\frac{1}{|\mathbf{k}'-\mathbf{q}-\mathbf{k}|\,\varepsilon_q \varepsilon_{|\mathbf{k}'-\mathbf{q}-\mathbf{k}|}}\right] \times \sum_{\sigma'=e,h}\frac{1}{\Delta+i\delta\varepsilon}\left[n_{k\sigma}n_{k'\sigma'}\left(1-n_{|\mathbf{k}'-\mathbf{q}|}\right)+(1-n_{k\sigma})(1-n_{k'\sigma'})\,n_{|\mathbf{k}'-\mathbf{q}|}\right] \tag{15a}$$

where

$$\delta\varepsilon = \varepsilon_{s\sigma} + \varepsilon_{|\mathbf{k}'-\mathbf{q}|\sigma'} - \varepsilon_{k\sigma} - \varepsilon_{k'\sigma'}$$

Equations (16) to (18) are exactly the same for continuous and discrete k, and the matrix elements appearing in those equations are

$$\left|\frac{M_{s_e,s_e}}{\hbar}\right|^2 = \left(\frac{\varepsilon_R}{\hbar}\right)^2\left(\frac{\hbar\omega_{LO}}{\varepsilon_R}\right)^{3/2}\alpha\, a_R\int_0^\infty dq e^{-q^2/(2\beta^2)}$$

$$\left|\frac{M_{s_e,\mathbf{k}}}{\hbar}\right|^2 = \left(\frac{\varepsilon_R}{\hbar}\right)^2\left(\frac{\hbar\omega_{LO}}{\varepsilon_R}\right)^{3/2} 2\alpha\,\frac{a_R}{\beta^2 A}\int_0^\infty dq\int_0^{2\pi} d\phi e^{-|\mathbf{k}+\mathbf{q}|^2/\beta^2}$$

$$\left|\frac{M_{\mathbf{k},\mathbf{k}'}}{\hbar}\right|^2 = \left(\frac{\varepsilon_R}{\hbar}\right)^2\left(\frac{\hbar\omega_{LO}}{\varepsilon_R}\right)^{3/2}\alpha\frac{a_R}{4A}\,\frac{1}{|\mathbf{k}-\mathbf{k}'|}\,8\pi$$

Input parameters (MKS):

N_{QD} is the quantum dot density in L^{-2}

β and q are in L^{-1}, A is in L^2

E_{dot} (electron) = 0.037eV below QW conduction bandedge

E_{dot} (hole) = 0.031eV above QW valence bandedge

QW subband effective masses = $0.067m_0$ (electrons), $0.180m_0$ (holes)

$\hbar\omega_{LO}$ = 0.036eV

$= 0.06$

$= 1.571 \times 10^{8} m^{-1}$

$a_r = 1.404 \times 10^{-8} m$

$_r = 0.00396 eV$

Appendix II: Publication and proposals

Refereed publications

1. S. Michael, W. W. Chow, H. C. Schneider, 'Coulomb corrections to the slowdown factor in quantum-dot quantum coherence,' Appl. Phys. Lett. **89**, 181114-1-3, 2006.
2. M. Lorke, W. W. Chow, T. R. Nielsen, J. Seebeck, P. Gartner and F. Jahnke, 'Anomaly in the excitation dependence of the optical gain of semiconductor quantum dots,' Phys. Rev. B 74, 035334 , 2006.
3. M. Lorke, F. Jahnke and W. W. Chow, 'Excitation dependences of gain and carrier-induced refractive index change in quantum-dot lasers**,'** Appl. Phys. Lett. **90** 051112, 2007.
4. W. W. Chow, S. Michael, H. C. Schneider, 'Many-body theory of quantum coherence in semiconductor quantum dots,' Journ. Modern Optics, 54, 2413-2424, 2007.
5. S. Michael, H. C. Schneider and W. W. Chow, 'Light propagation with quantum-coherence induced group-velocity slowdown in semiconductor quantum dots,' (in preparation).

Invited talks

1. W. W. Chow, 'Many-body corrections to group-velocity slowdown in quantum dots,' Winter Colloquium on the Physics of Quantum Electronics (PQE), 1/3-6/07, Snowbird, UT.
2. W. W. Chow, 'Coherence and dephasing in semiconductor quantum dots,' Princeton-TAMU Symposium on Quantum Coherence and Laser Spectroscopy, 3/16-17/07, Princeton, NJ.
3. W. W. Chow, M. Lorke and F. Jahnke, 'Gain and refractive index in quantum-dot lasers,' Montana Meeting on Fundamental Optical Processes in Semiconductors (FOPS), 7/23-27/07, Big Sky, MT.
4. W. Chow, Optical properties of semiconductor quantum dots, IEEE PhotonicsGlobal@Singapore 2008 Dec. 8 -11, 2008, Singapore.
5. W. W. Chow, 'Studies on the relative advantages of quantum-dot and quantum-well gain media in lasers and amplifiers' CLEO 09, May 31-June5, 2009, Baltimore.

Presented talk

S. Michael, W. W. Chow, H. C. Schneider, 'Coulomb Corrections to the Slow-Down Factor in Quantum-Dot Quantum Coherence,' CLEO-Europe 2007, 6/17-22/07, Munich, Germany.

Proposals (funded)

1. 08-1220, 'Injection-locked composite lasers for mm-wave modulation,' Vawter (PI) – 3 years, $1300K.
2. 08-1225, ‘Efficient multi-exciton emission from quantum dots,’ Luk (PI) – 3 years, $1700K.
3. 08-0346, ‘Four-wave mixing for phase-matching-free nonlinear optics in quantum cascade structures,’ Chow (PI) – 3 years, $1200K.

Proposals (unfunded)

1. 09-0135, 'Electromagnetically induced chirality: negative refraction without metamaterials' Chow (PI)
2. 09-0657, ' Room temperature GaN polariton light source,' Fischer (PI)

Proposals (pending)

1. 'Exceeding conventional thermo-photovoltaic solar-energy conversion limit with negative-refraction metallic photonic crystal,' BES Basic Research for Solar Energy Utilization
2. 'Tailored light-matter interaction,' thrust 4 of the EFRC BES proposal
3. 'Investigation of strong light matter interactions in solid state systems, ' Single Investigator/Small Group Research preproposal BES
4. 'Exceeding the solar PV fundamental limit by coherent energy transfer,' Single Investigator/Small Group Research preproposal BES
5. 'Nanostructure Solar Energy Conversion Center,' ASU DOE BES EFRC

Coulomb corrections to the slowdown factor in quantum-dot quantum coherence

S. Michael
Physics Department, Kaiserslautern University, P.O. Box 3049, 67653 Kaiserslautern, Germany

W. W. Chow
Sandia National Laboratories, Albuquerque, New Mexico 87185-1086

H. C. Schneider[a)]
Physics Department, Kaiserslautern University, P.O. Box 3049, 67653 Kaiserslautern, Germany

(Received 1 June 2006; accepted 6 September 2006; published online 1 November 2006)

Quantum-coherence induced group-velocity slowdown in a semiconductor quantum-dot structure is investigated using a many-body theory. The predictions are found to be noticeably different from those obtained in the independent-particle treatment typically used for describing atomic quantum coherence. In particular, Hartree-Fock renormalizations can lead to over two orders of magnitude reduction in the predicted pump intensity requirement for group-velocity slowdown to occur. Results are presented for the slowdown factor and slowdown-bandwidth product in a pulsed InAs–GaAs quantum-dot Λ scheme. © *2006 American Institute of Physics*. [DOI: 10.1063/1.2364164]

Research on quantum-coherence effects in atomic systems[1,2] has stirred interest in possible optoelectronic applications. An example is optical buffers based on the slow-light phenomenon.[3,4] To realize this goal, physics and device engineering issues are being addressed in the context of a condensed-matter system. For instance, excitonic or spin correlations leading to electromagnetically induced transparency (EIT) in semiconductor quantum wells (QWs) were investigated experimentally or theoretically.[5–7] There is also interest in quantum coherences using quantum dots (QDs),[8,9] because of reports of long dephasing times[10] and preservation of atomiclike properties (e.g., discrete energy levels) at high temperatures.

Several ideas for quantum coherence in QDs are being proposed and analyzed. However, the analyses are mostly adapted from atomic quantum-coherence theory, where many-body effects are neglected.[8,11] To improve on these analyses, this letter investigates QD quantum coherence using the semiconductor Bloch equations, modified to allow the tracking of the additional optical fields and electron-hole polarizations in a Λ system.[9] Furthermore, a relatively detailed description of the electronic states of a coupled QD-QW system is included, together with the coupling of these states via collisions in the relaxation rate approximation. A treatment in the framework of semiconductor Bloch equations (Hartree-Fock) neglects excitonic correlations, which have been shown to be important for the *incoherent* emission from QDs and at lower temperatures.[12] However, in the temperature range considered in the present letter, the semiconductor Bloch equations are expected to provide a good description of the influence of the Coulomb interaction on the quantum-coherence properties of a QD ensemble.

A structure consisting of InAs QDs embedded in a GaAs QW is chosen for the study. The electronic level structure[13] is computed for InAs pyramidal dots (each with a base of 12×12 nm^2 and height of 6 nm) and wetting layer of thickness of 1 nm. There are three confined electron and six confined hole levels, denoted by $|e0\rangle$ to $|e2\rangle$ and $|h0\rangle$ to $|h5\rangle$. This is in agreement with previous calculations, e.g., Ref. 14, where input material parameters are listed. Each level is doubly degenerate. The level energies and dipole selection rules give rise to a modified Λ configuration, with the drive field connecting $|e0\rangle$ and $|h0\rangle$ and a probe field connecting the transitions $|e0\rangle$ and $|h1\rangle$, as well as $|e0\rangle$ and $|h2\rangle$. The other QD and QW states in Fig. 1 are coupled to one another and to the states in the Λ configuration via collisions.

In describing the theoretical formulation, we will highlight the many-body aspect, because the Coulomb corrections are the focus of this letter and because the semiconductor equations of motion have basically similar forms as the corresponding atomic ones. For example, the semiconductor equation of motion for the polarization connecting the states $|e0\rangle$ and $|h1\rangle$ is

$$\frac{dp_{e0,h1}}{dt} = -(i\omega_{e0,h1} + \gamma^d)p_{e0,h1} - i\Omega_{e0,h1}(n_{e0} + n_{h1} - 1) + i\sum_{\beta\neq h1}{}'\Omega_{e0,\beta}p_{\beta,h1} - i\sum_{\beta\neq h1}{}'\Delta_{h1,\beta}p_{e0,\beta}, \quad (1)$$

where the first line is similar to the atomic polarization equation of motion. In the above equation, γ^d is the dephasing rate, n_j is population in level j, and the primed summations are over hole states that are connected to electron-hole coherences that are closely resonant with the drive and probe fields. The differences are the additional term appearing in the second line and the carrier-density dependent renormalizations of the transition frequency $\omega_{e0,h1}=\omega^{(0)}_{e0,h1}+\Delta_{e0}+\Delta_{h1,h1}$ and Rabi frequency $\Omega_{e0,h1}=\frac{\mu_{e0,h1}}{2\hbar}E_p e^{-i\omega_p t}+\Delta_{e0,h1}$, where $\omega^{(0)}_{e0,h1}$ and $\mu_{e0,h1}$ are the transition frequency and dipole matrix element determined from the single-particle electronic-structure calculation, respectively, and E_p is the probe field with frequency ω_p. The many-body contributions, which may be grouped into electron, hole-hole, and electron-hole terms, are

$$\hbar\Delta_{e0} = -\sum_{\alpha}(V^{e0,e0}_{\alpha,\alpha} - V^{e0,\alpha}_{e0,\alpha})n_\alpha - \sum_{\beta}V^{e0,\beta}_{e0,\beta}n_\beta - \sum_{k}V^{e0,e0}_{kk}n^e_k, \quad (2)$$

a)Electronic mail: hcsch@physik.uni-kl.de

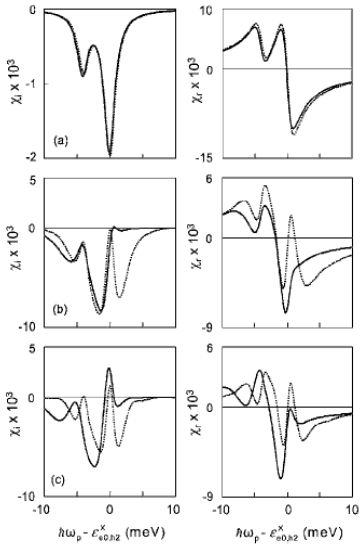

FIG. 1. Imaginary (left) and real (right) parts of susceptibility vs probe energy. The solid and dashed curves are the many-body and independent-particle results, respectively. To display spectra corresponding to unexcited system, complete EIT and maximum LWI, the times for the many-body (independent-particle) spectra are −2 (−2) ps (a), 0.11 (−0.10) ps (b), and 0.42 (0.16) ps (c) relative to the maximum of drive pulse. The probe energy detuning is relative to the zero-density $e0$-$h2$ exciton resonance and the independent-particle spectra are shifted to facilitate comparison of the line shapes.

$$\hbar\Delta_{h1,\beta} = -\sum_{\beta'}(V^{\beta,h1}_{\beta'\beta'} - V^{\beta,\beta'}_{h1,\beta'})n_{\beta'} - \sum_{\alpha} V^{\beta,\alpha}_{h1,\alpha} n_{\alpha} - \sum_{k} V^{\beta,h1}_{kk} n^{h}_{k} + {\sum_{\beta',\beta''}}' (V^{\beta,h1}_{\beta'\beta''} - V^{\beta,\beta''}_{h1,\beta'}) p_{\beta'\beta''}, \quad (3)$$

$$\hbar\Delta_{e0,h1} = {\sum_{\beta}}' V^{e0,h1}_{e0,\beta} p_{e0,\beta}, \quad (4)$$

respectively, where the summation index α refers to QD electron states, β' and β'' ($\neq\beta'$) to QD hole states, and k to QW states. Each term on the right-hand contains matrix elements[9] of the Coulomb interaction energy $V^{\alpha\beta}_{\alpha'\beta'} = \int \phi^*_{\alpha}(\mathbf{r})\phi^*_{\beta}(\mathbf{r}')e^2/4\pi\varepsilon_b|\mathbf{r}-\mathbf{r}'|\phi_{\beta'}(\mathbf{r}')\phi_{\alpha'}(\mathbf{r})d^3r d^3r'$. We use a many-body theory where screening effects arise from the changes in the dielectric function due to the presence of carriers in the QW states.[15] For the situations considered in this letter, the QW carrier population is negligible because of the relatively deep InAs quantum-dot confinement. Therefore, we neglected the plasma screening contributions in the above equations. Also neglected are the microscopic dephasing processes that couple the polarization of interest to other polarizations, giving rise to nondiagonal scattering contributions. A recent study showed that these contributions are usually small in QDs because of the three-dimensional confinement.[16] Consequently, dephasing effects are approximated by the diagonal term in Eq. (1) containing the effective dephasing rate γ^d.

For the populations, one has, e.g.,

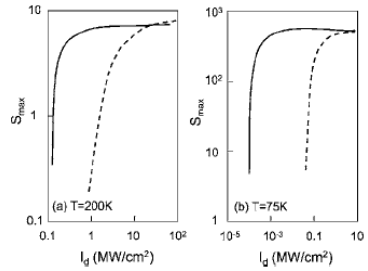

FIG. 2. Maximum slowdown factor vs drive-pulse peak intensity for lattice temperatures of 200 K (a) and 75 K (b). The solid and dashed curves are the many-body and independent-particle results, respectively.

$$\frac{dn_{e0}}{dt} = i{\sum_{\beta}}'(\Omega_{e0,\beta}p_{\beta,e0} - p_{e0,\beta}\Omega_{\beta,e0}) - \gamma^d_{c\text{-}c}[n_{e0} - f_{e0}(\mu^p_e, T_p)] - \gamma^d_{c\text{-}p}[n_{e0} - f_{e0}(\mu^l_e, T_l)], \quad (5)$$

where $\gamma^d_{c\text{-}c}$ and $\gamma^d_{c\text{-}p}$ are carrier-carrier scattering and carrier-phonon scattering rates, respectively. Besides $\Omega_{\alpha,\beta}$, the difference between semiconductor and atomic equations lies in the population relaxation. In our case, we have terms approximating the collision-induced particle exchange processes that drive the population distributions to quasiequilibrium Fermi-Dirac functions f_i at chemical potentials and temperatures (μ^p_i, T_p) and (μ^l_i, T_l), where T_p and T_l are the plasma and lattice temperatures, respectively. The details of the computational procedure are given elsewhere.[9]

We begin by considering an experiment where an optical pulse is incident on the QD sample to drive the polarization $p_{e0,h0}$. The optical response to this excitation is investigated by examining the complex susceptibility seen by a probe field that is closely resonant with the polarizations $p_{e0,h1}$ and $p_{e0,h2}$. The numerical computations involve solving 36 polarization equations of motion [of the form (1)], together with nine equations of motion for the QD populations [of the form (5), four with optical interaction and five without] and around 100 equations of motion for the populations in the momentum-resolved QW electron and hole states. The complex susceptibility at some time and probe frequency is computed from the polarizations $p_{e0,h1}$ and $p_{e0,h2}$, according to semiclassical laser theory.

For the results shown in Fig. 1, we use a sech drive pulse with peak intensity of 1.4 MW/cm^2 and duration [full width half maximum (FWHM)] of 1.7 ps. Furthermore, the dot density is $N_d = 5\times10^{10}$ cm^{-2} and lattice temperature $T_l = 200$ K, where recent literature[8,17] gives scattering rates around $\gamma^d = 1.5\times10^{12}$ s^{-1}, $\gamma_{c\text{-}c} = 2\times10^{12}$ s^{-1}, and $\gamma_{c\text{-}p} = 2\times10^{11}$ s^{-1}. The solid curves describe the imaginary (χ_i, left column) and real (χ_r, right column) parts of the susceptibility as functions of probe frequency and at different times ($t=0$ is chosen to be at the peak of the drive pulse). Prior to the excitation, one has the typical excitonic absorption resonances approximately centered at the unexcited $e0$-$h1$ and $e0$-$h2$ exciton resonances and corresponding dispersions as given by the Kramers-Kronig relations [Fig. 1(a)]. Figures 1(b) and 1(c) are for times when complete transparency and maximum gain are created by EIT and lasing without inversion (LWI), respectively, at the $e0 \rightarrow h2$ transition. For times longer than the reciprocal of the dephasing rate, the quantum-coherence effects vanish and the spectral shapes re-

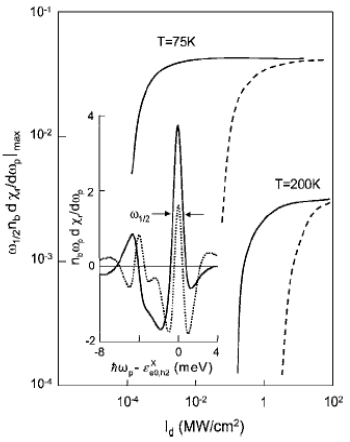

FIG. 3. Maximum slowdown-bandwidth product vs drive-pulse peak intensity for lattice temperatures of 75 K and 200 K. The inset shows a $n_b\omega_p d\chi_r/d\omega_p$ spectrum for both treatments. The solid and dashed curves are the many-body and independent-particle results, respectively.

turn to forms of Fig. 1(a), except for amplitude changes due to carrier creation and population of excited states.

Also plotted in Fig. 1 dashed curves) is the result obtained by ignoring the Coulomb renormalizations and population redistribution, i.e., by setting to zero, $\gamma_{c\text{-}c}$, $\gamma^a_{c\text{-}c}$, $\gamma_{c\text{-}p}$, $\gamma^a_{c\text{-}p}$, and the right-hand side of Eqs. (2)–(4). This gives the independent-particle (atomic) result with absorption resonances centered at $\omega^{(0)}_{e0,h1}$ and $\omega^{(0)}_{e0,h2}$. To reach complete transparency, a much higher drive-pulse peak intensity of 21.9 MW/cm^2 is necessary in this case. The time evolution of the probe susceptibility is different from that of the many-body case. Consequently, the times for complete transparency and maximum gain in the $e0 \rightarrow h2$ transition are different, as indicated in the caption of the figure. Comparison of solid and dashed curves indicates that appreciable differences can occur between the two descriptions. The many-body corrections give rise to asymmetries in the resonances and different spectral peak amplitudes.

A consequence of the differences between the present theory and the independent-particle treatment, as depicted in Fig. 1, is in the prediction of the slowdown factor $S=n_b(1+\omega_p d\chi_r/d\omega_p)$. The slowdown factor, which is a measure of the refractive index changes resulting in optical group-velocity reduction, is of interest for applications such as optical storage. To show explicitly the discrepancy, Fig. 2 plots the maximum value for S as a function of drive intensity for lattice temperatures T_l=75 and 200 K. For T_l=75 K, the dephasing rate is taken to be $\gamma^d = 1.5\times10^{11}$ s^{-1},[8,17] and a sech drive pulse with FWHM of 8.3 ps is used. There is clearly a strong temperature dependence in the slowdown factor. However, independent of temperature, there are appreciable differences between many-body and independent-particle predictions (compare solid and dashed curves). Most important of these differences is the over two orders of magnitude overestimation of the necessary drive-pulse intensity when the many-body renormalizations are neglected. Also, while both treatments predict basically the same maximum achievable S, the drive intensities for reaching saturation are drastically different. Detailed analysis reveals that the Coulomb enhancement is the primary cause for these differences.

Important for pulse propagation is the slowdown-bandwidth product.[18] The differences between solid and dashed curves in Fig. 1 also suggest that this product will be quite different between the two treatments. The inset in Fig. 3 shows the spectra of $n_b\omega_p d\chi_r/d\omega_p$ at 200 K for drive intensity of 5.5 MW/cm^2 and time when the maximum slowdown factor is reached. The solid and dashed curves are obtained using the many-body and independent-particle descriptions, respectively. From such spectra, we obtain the product $\omega_{1/2} n_b d\chi_r/d\omega_p$, where $\omega_{1/2}$ is the FWHM of the $e0 \rightarrow h2$ resonance. Again, comparison of solid and dashed curves shows significant many-body contributions.

In conclusion, quantum coherence in a semiconductor QD structure is studied by using a many-body theory to calculate the optical response of a pulse-driven Λ system. The present theory differs from the typical independent-particle treatment by taking into account Hartree-Fock renormalizations, the details of the QD and QW states, and their coupling via collisions. The slowdown factor and slowdown-bandwidth product, which characterize device performance in an optical buffer, are calculated, and the results are compared to the independent-particle treatment. It is found that the predictions for these quantities differ significantly for the two approaches. When many-body effects are neglected, one seriously overestimates the drive intensity requirement for quantum coherence to occur.

This work was supported by the U.S. Department of Energy under Contract No. DE-AC04-94AL85000, the Humboldt Foundation, and a CPU time grant from the NIC at the Forschungszoutrumjülich.

[1] S. E. Harris, J. E. Field, and A. Imamoglu, Phys. Rev. Lett. **64**, 1107 (1990).
[2] M. O. Scully, S. Y. Zhu, and A. Gavrielides, Phys. Rev. Lett. **62**, 2813 (1989).
[3] L. V. Hau, S. E. Harris, Z. Dutton, and C. H. Behroozi, Nature (London) **397**, 594 (1999).
[4] D. F. Phillips, A. Fleischhauer, A. Mair, and R. L. Walsworth, Phys. Rev. Lett. **86**, 783 (2001).
[5] M. Phillips and H. L. Wang, Phys. Rev. Lett. **89**, 186401 (2002).
[6] Z. S. Yang, N. H. Kwong, R. Binder, and A. L. Smirl, J. Opt. Soc. Am. B **22**, 2144 (2005).
[7] S. Sarkar, P. Palinginis, P. C. Ku, C. J. Chang-Hasnain, N. H. Kwong, R. Binder, and H. Wang, Phys. Rev. B **72**, 035343 (2005).
[8] C. J. Chang-Hasnain, P. C. Ku, J. Kim, and S. L. Chuang, Proc. IEEE **91**, 1884 (2003).
[9] W. W. Chow, H. C. Schneider, and M. C. Phillips, Phys. Rev. A **68**, 053802 (2003).
[10] P. Borri, W. Langbein, S. Schneider, U. Woggon, R. L. Sellin, D. Ouyang, and D. Bimberg, Phys. Rev. Lett. **87**, 157401 (2001).
[11] A. A. Belyanin, F. Capasso, V. V. Kocharovsky, and M. O. Scully, Phys. Rev. A **63**, 053803 (2001).
[12] N. Baer, C. Gies, J. Wiersig, and F. Jahnke, Eur. Phys. J. B **50**, 411 (2006).
[13] NEXTNANO^3 device simulator, http://www.wsi.tum.de/nextnano
[14] O. Stier, M. Grundmann, and D. Bimberg, Phys. Rev. B **59**, 5688 (1999).
[15] H. C. Schneider, W. W. Chow, and S. W. Koch, Phys. Rev. B **64**, 115315 (2001).
[16] H. C. Schneider, W. W. Chow, and S. W. Koch, Phys. Rev. B **70**, 235308 (2004).
[17] P. Borri, W. Langbein, S. Schneider, U. Woggon, R. L. Sellin, D. Ouyang, and D. Bimberg, IEEE J. Sel. Top. Quantum Electron. **8**, 984 (2002).
[18] Z. J. Deng, D. K. Qing, P. Hemmer, C. H. R. Ooi, M. S. Zubairy, and M. O. Scully, Phys. Rev. Lett. **96**, 023602 (2006).

Anomaly in the excitation dependence of the optical gain of semiconductor quantum dots

M. Lorke,[1,*] W. W. Chow,[2] T. R. Nielsen,[1] J. Seebeck,[1] P. Gartner,[1] and F. Jahnke[1]
[1]*Institute for Theoretical Physics, University of Bremen, 28334 Bremen, Germany*
[2]*Semiconductor Materials and Device Science Department, Sandia National Laboratories, Albuquerque, New Mexico 87185-0601, USA*
(Received 2 February 2006; revised manuscript received 21 June 2006; published 26 July 2006)

Optical gain behavior of semiconductor quantum dots is studied within a quantum-kinetic theory, with carrier-carrier and carrier-phonon scattering treated using renormalized quasiparticle states. For inhomogeneously broadened samples, we found the excitation dependence of gain to be basically similar to quantum-well and bulk systems. However, for a high quality sample, our theory predicts the possibility of a decreasing peak gain with increasing carrier density. This anomaly can be attributed to the delicate balance between state filling and dephasing.

DOI: 10.1103/PhysRevB.74.035334 PACS number(s): 78.67.Hc, 71.35.Cc

I. INTRODUCTION

Semiconductor quantum dots (QDs) are currently under intense investigation because of scientific and engineering interests. They are considered as key materials for next generation optoelectronic devices. New applications emerge also in the fields of semiconductor quantum optics with fundamental studies of light-matter interaction[1–3] and for quantum information processing.[4,5] A central issue in various applications is the role of dephasing due to intrinsic interaction processes. Dephasing limits the quantum coherence and determines the homogeneous emission linewidth of QDs.

Crucial to the analysis of fundamental experiments and the realization of engineering advantages is the knowledge of intrinsic QD behavior and the understanding of underlying physics. Extracting the information experimentally is challenging because sample inhomogeneities make the separation of intrinsic from extrinsic properties difficult. Theoretical investigations have been hindered by the lack of a predictive theory. Recently, this hurdle was removed by the development of the elements for a microscopic theory that allows a rigorous treatment of dephasing. These theoretical tools enable the systematic study of fundamental QD behavior. In this paper, we demonstrate the role of intrinsic interaction processes and the resulting excitation induced dephasing for optical absorption and gain spectra. The results are not only of direct relevance for QD lasers but also for other QD applications. On a general level, the role of various interaction processes is quantified. On a more particular level, anomalies in the excitation dependent emission properties are addressed, which are not known both in higher-dimensional semiconductor structures and in atomic systems. Our investigations are performed for typical self-assembled QDs, where the Coulomb interaction of carriers and the carrier-phonon interaction leads to a coupling (i) between the discrete QD states and (ii) to a quasicontinuum of quantum well (QW) delocalized states, e.g., from a wetting layer.

Polarization dephasing directly influences the amplitude and spectral broadening of optical absorption and gain. The primary sources for dephasing are carrier-carrier and carrier-phonon scattering. These processes also contribute to carrier capture and relaxation, which are important for an efficient device operation. The Coulomb interaction leading to carrier-carrier scattering provides efficient scattering channels, especially at elevated carrier density and temperature.[6–8] On the other hand, there was concern over the interaction of carriers with longitudinal optical (LO) phonons, which provides additional scattering channels and thermalization of carrier population. Calculations based on perturbation theory predicted strongly inhibited carrier-LO-phonon scattering, because of mismatch between QD levels and LO-phonon energy.[9] This led to the belief that the QD device performance would be degraded because of a phonon bottleneck problem.[10]

Later, nonperturbative treatments within the polaron picture indicated a less serious phonon bottleneck problem,[11] consistent with many experiments, see Ref. 12. A recent quantum-kinetic treatment of carrier-phonon interaction in the polaron picture clearly demonstrates efficient carrier-LO-phonon scattering.[12] This development together with a non-Markovian treatment of polarization dephasing due to carrier-carrier scattering within a QD-QW system[13] allow the completion of a truly predictive theory for QD optical response. The resulting formalism contains a detailed accounting of electronic structure effects and a microscopically consistent treatment of the many-body interaction. The many-body effects include the Hartree-Fock energy renormalizations (band-gap shrinkage and Coulomb enhancement) which contribute to shifts and amplitude modifications of QD absorption and emission resonances, and polarization dephasing due to carrier-carrier and carrier-LO-phonon scattering, which is responsible for the intrinsic (homogeneous) broadening of these resonances and additional energy shifts. Our investigation is based on this QD optical response theory.

We begin by describing the calculation of optical absorption and gain for a sample with a uniform QD size and composition. The computed properties are customarily referred to as being associated with the homogeneously broadened or intrinsic situation. Then, we discuss the incorporation of inhomogeneously broadening effects, such as those arising from QD size and composition variations. This allows one to transform from intrinsic behaviors to what is observed in present experiments. The availability of scattering channels contributing to polarization dephasing depends on the discrete QD energy level spacings, which in turn, depend on the QD confinement potential. By considering $In_{0.3}Ga_{0.7}As$ and

InAs QDs embedded in GaAs QWs, we are able to examine the two very different scenarios of shallow and deep quantum confinement. For these two structures, the focus is on two questions, involving the homogeneously broadened gain spectrum (especially the intrinsic spectral shape and width) and the spectral changes with carrier density. A rigorous treatment of scattering is necessary for addressing these problems. The typical QD gain calculation, which uses the relaxation rate approximation, cannot tell us about the homogeneously broadened spectrum, because it assumes a line shape function and treats the spectral width as a free parameter. A central result of this paper is the discovery of an anomaly in the excitation dependence of QD gain: a decrease in peak gain with increasing carrier density. This result will directly influence QD applications under high excitation conditions. The behavior arises from a delicate balancing of state filling and dephasing, so that a detailed treatment of the carrier density dependence of scattering processes is necessary. Again, this can only be accomplished with the recent quantum-kinetic developments.

II. THEORETICAL DESCRIPTION OF QUANTUM-DOT GAIN SPECTRA

The gain calculation starts with solving for the microscopic polarization p_α, where α represents the discrete levels ν in QD transitions and the in-plane carrier momentum $\mathbf{k}$ in QW transitions. In our confinement situation it is sufficient to consider only the lowest QW subband for gain calculations. Working in the Heisenberg picture and using a many-particle Hamiltonian that includes carrier-carrier interaction, carrier-phonon interaction, and dipole interaction between electron-hole pairs and laser field, the Fourier-transformed polarization equation is[14]

$$(\hbar\omega - \varepsilon_\alpha^e - \varepsilon_\alpha^h)p_\alpha + \hbar\Omega_\alpha(1 - n_\alpha^e - n_\alpha^h) = iS_\alpha^{c-c}(\omega) + iS_\alpha^{c-p}(\omega). \tag{1}$$

In (1), the Rabi energy $\hbar\Omega_\alpha$ and transition energy ε_α^β ($\beta = e,h$) contain the single-particle electronic structure properties and the many-body Hartree-Fock contributions. The complex Coulomb correlation (scattering) term $S_\alpha^{c-c}(\omega)$ is treated in the second Born approximation and non-Markovian limit[13] using self-consistently renormalized energies for the scattering partners.[14] For the carrier-phonon correlation $S_\alpha^{c-p}(\omega)$ we assume the random-phase approximation and use the Fröhlich coupling to monochromatic LO phonons to determine the QD polaron renormalization of the electronic states.[11,12] For linear optical response to a weak laser probe field $E(\omega)$ at frequency ω, the carrier distribution n_α^β is to a good approximation a Fermi-Dirac function. A typical calculation involves simultaneously solving a set of 100–150 equations, each of the form given by (1) and coupled to one another by nondiagonal terms in Ω_α, $S_\alpha^{c-c}(\omega)$and $S_\alpha^{c-p}(\omega)$. The solution is used to give the homogeneously broadened (intrinsic) optical gain of the QD-QW structure:

$$g(\omega) = -\frac{K}{\varepsilon w E(\omega)}\,\mathrm{Im}\left[N_{dot}\sum_\nu \mu_\nu p_\nu(\omega) + \frac{1}{A}\sum_{\mathbf{k}} \mu_{\mathbf{k}} p_{\mathbf{k}}(\omega)\right], \tag{2}$$

where ε is the background permittivity, K is the laser field wave vector in the medium, w is the QW width, and N_{dot} is the sheet density of QDs in a QW of area A. The spectral width calculated using (1) and (2) depends solely on dephasing processes described by the real part of the correlation contributions $S_\alpha^{c-c}(\omega)$ and $S_\alpha^{c-p}(\omega)$. Experimental data suggest that present QD gain regions are inhomogeneously broadened by QD size and composition variations. To incorporate these deviations from a perfect situation, we follow gas laser theory,[15] and perform a statistical average of the homogeneous gain spectra assuming an inhomogeneous width, σ_{inh}.

We begin by considering the case of $In_{0.3}Ga_{0.7}As$ QDs embedded in a 4 nm thick GaAs quantum well, which is cladded by $Al_{0.2}Ga_{0.8}As$ layers. To compute the electronic structure, the actual QD shape is approximated by a disk of height and diameter 2 and 18 nm, respectively. Assuming appreciably weaker QD confinement in the QW plane than in perpendicular direction,[16] it is possible to separate the problem into radial and vertical components. With this simplification, the electronic structure for the QD-QW system can already be computed, using as input the bulk material properties, such as the electron effective masses and Luttinger parameters, spin-orbit energy splitting, elastic constants, lattice constants, and deformation potentials.[17] The solutions contain the effects of quantum confinement and mixing between hole states. For the QW states, we use orthogonalized plane waves.[8] The calculation indicates one localized electronic state and one localized hole state located 15 and 25 meV, respectively, below their respective QW band edges. While there are more rigorous approaches to determining the QD single-particle states,[16] the present method adequately describes the essential features necessary for our study of excitation effects in optical response.

III. RESULTS

Figure 1(a) shows the homogeneously broadened gain spectra computed using (1) and (2). The curves are for $T = 300$ K and different carrier densities, which are defined as $N = 2N_{dot}\Sigma_i n_i^e + 2A^{-1}\Sigma_{\mathbf{k}} n_{\mathbf{k}}^e = 2N_{dot}\Sigma_i n_i^h + 2A^{-1}\Sigma_{\mathbf{k}} n_{\mathbf{k}}^h$. For the shallow QD structure, each spectrum has an *s*-shell resonance and a broad QW contribution. Figure 1(b) depicts the corresponding inhomogeneously broadened spectra. By assuming an inhomogeneous broadening of $\sigma_{inh} = 20$ meV, the spectra in Fig. 1(b) resemble closely those observed in experiment.[18] Comparison of the two sets of spectra reveals significant masking of intrinsic QD properties by QD size and composition variations in present experiments. The homogeneously broadened result clearly indicates a carrier-density dependent energy shift in the QD resonances. There is also noticeable spectral broadening of QD resonances with increasing carrier density, suggesting a strong excitation dependence in the dephasing. Both effects were observed in QD luminescence in single-dot experiments, but not at car-

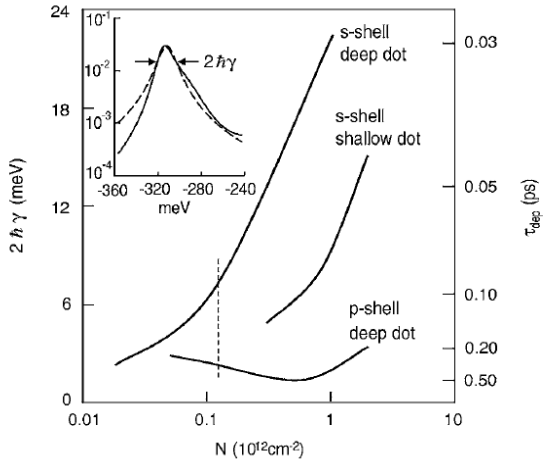

FIG. 3. Full width at half height (FWHH) of QD resonances versus carrier density. The inset shows a typical QD resonance and best fit with a Lorentzian function.

at $N=5\times10^{11}$ cm^{-2}. Comparison with a Lorentzian function with the same amplitude maximum and FWHH (dashed curve) indicates a basically good fit except for the asymmetry in the actual resonance and deviations at the spectral tails. The differences may be traced to the nondiagonal correlation contributions and QW influence. The main curves indicate significant variation in dephasing with carrier density and QD structure. For the shallow QD, the *s*-shell dephasing increases appreciably with carrier density. For the deep QD, there is a further complication of the *s*- and *p*-shell resonances experiencing different dephasing effects. When g_{pk} moves from the *s*-shell to the *p*-shell resonance (intersection of solid curve and dashed line), there is a sharp decrease in dephasing. The *p*-shell dephasing dependence on carrier density first decreases before increasing, with the increase caused by the onset of QW contributions. The dephasing widths or times (right axis) is consistent with experiment.[20] The complex dependences shown in the figure are describable only with a rigorous treatment of scattering effects.

IV. SUMMARY

The intrinsic properties of QD gain is investigated within the context of a microscopic theory, with carrier correlations treated at the level of quantum kinetics. It was found that a QD active medium exhibits unique optical gain properties that are usually masked by inhomogeneous broadening. The most interesting is the decrease in peak gain with increasing excitation for certain carrier density ranges. This anomalous behavior depends on the delicate balancing of band-filling and dephasing contributions in a Coulomb coupled QD-QW system.

ACKNOWLEDGMENTS

The work was supported by the Deutsche Forschungsgemeinschaft, NIC of Forschungszentrum Jülich, U. S. Department of Energy under Contract No. DE-AC04-94AL85000, and Humboldt Foundation.

*Electronic address: www.itp.uni-bremen.de

[1] M. Bayer, F. Weidner, A. Larionov, A. McDonald, A. Forchel, and T. L. Reinecke, Phys. Rev. Lett. **86**, 3168 (2001).
[2] J. P. Reithmaier, G. Sek, A. Löffler, C. Hofmann, S. Kuhn, S. Reitzenstein, L. V. Keldysh, V. D. Kulakovskii, T. L. Reinecke, and A. Forchel, Nature (London) **432**, 197 (2004).
[3] T. Yoshie, A. Scherer, J. Hendrickson, G. Khitrova, H. M. Gibbs, G. Rupper, C. Ell, O. B. Shchekin, and D. G. Deppe, Nature (London) **432**, 200 (2004).
[4] P. Michler, A. Imamoglu, M. D. Mason, P. J. Carson, G. F. Strouse, and S. K. Buratto, Nature (London) **406**, 968 (2000).
[5] X. Q. Li, Y. W. Wu, D. Steel, D. Gammonand, T. H. Stievaterand, D. S. Katzer, D. Park, C. Piermarocchi, and L. J. Sham, Science **301**, 809 (2003).
[6] U. Bockelmann and T. Egeler, Phys. Rev. B **46**, 15574 (1992).
[7] I. Magnusdottir, S. Bischoff, A. V. Uskov, and J. Mørk, Phys. Rev. B **67**, 205326 (2003).
[8] T. R. Nielsen, P. Gartner, and F. Jahnke, Phys. Rev. B **69**, 235314 (2004).
[9] H. Benisty, C. M. Sotomayor-Torres, and C. Weisbuch, Phys. Rev. B **44**, 10945 (1991).
[10] M. Sugawara, K. Mukai, and H. Shoji, Appl. Phys. Lett. **71**, 2791 (1997).
[11] T. Inoshita and H. Sakaki, Phys. Rev. B **56**, R4355 (1997).
[12] J. Seebeck, T. R. Nielsen, P. Gartner, and F. Jahnke, Phys. Rev. B **71**, 125327 (2005).
[13] H. C. Schneider, W. W. Chow, and S. W. Koch, Phys. Rev. B **70**, 235308 (2004).
[14] M. Lorke, T. R. Nielsen, J. Seebeck, P. Gartner, and F. Jahnke, Phys. Rev. B **73**, 085324 (2006).
[15] J. W. E. Lamb, Phys. Rev. **134**, A1429 (1964).
[16] A. D. Andreev and E. P. O'Reilly, Phys. Rev. B **62**, 15851 (2000).
[17] *Numerical Data and Functional Relationships in Science and Technology*, Landolt-Börnstein (Springer-Verlag, Berlin, 1982), Vol. 17.
[18] S. Osborne, P. Blood, P. Smowton, J. Lutti, Y. C. Xin, A. Stintz, D. Huffaker, and L. Lester, IEEE J. Quantum Electron. **40**, 1639 (2004).
[19] K. Matsuda, K. Ikeda, T. Saiki, H. Saito, and K. Nishi, Appl. Phys. Lett. **83**, 2250 (2003).
[20] P. Borri, W. Langbein, J. M. Hvam, F. Heinrichsdorff, M. H. Mao, and D. Bimberg, IEEE J. Sel. Top. Quantum Electron. **6**, 544 (2000).

Excitation dependences of gain and carrier-induced refractive index change in quantum-dot lasers

M. Lorke[a] and F. Jahnke
Institute for Theoretical Physics, University of Bremen, 28334 Bremen, Germany

W. W. Chow
Semiconductor Materials and Device Science Department, Sandia National Laboratories, Albuquerque, New Mexico 87185-0601; Physics Department, Texas A&M University, College Station, Texas 77843; and Institute of Quantum Studies, Texas A&M University, College Station, Texas 77843

(Received 29 November 2006; accepted 3 January 2007; published online 2 February 2007)

The excitation-density dependence of optical gain and refractive index changes in quantum-dot active media is investigated on the basis of a microscopic theory. Carrier-carrier Coulomb interaction and carrier-phonon interaction are treated on the level of a quantum-kinetic description. In the range of small optical gain the authors find small values of the α factor, while in the regime of gain saturation $|\alpha|$ increases drastically. © *2007 American Institute of Physics*.
[DOI: 10.1063/1.2437670]

The advantages of semiconductor quantum-dot (QD) lasers are being intensively studied and discussed. Low transparency carrier density, high differential gain, and small carrier-induced refractive index change have been predicted.[1] For laser devices, these gain medium properties translate to low threshold currents, temperature-insensitive performance, suppression of filamentation, and reduced sensitivity to optical feedback, all of which have been experimentally demonstrated.[2–5] Some questions remain, e.g., the extent to which high-speed modulation characteristics can be better than quantum-well (QW) lasers.[6] A first step towards answering this question is knowledge of the excitation dependences of gain and carrier-induced refractive indices. The former helps determine the modulation bandwidth, while the latter controls the noise characteristics from frequency chirp and laser linewidth.

The beneficial QD gain and refractive index properties are linked to the discrete nature of the energy spectrum associated with localized carrier states. Application of a simple atomlike (i.e., noninteracting two-level system) description predicts symmetric absorption and gain resonances, as well as the absence of carrier-induced refractive index change at the resonance peaks. While the atomlike description is an acceptable approximation in many situations, such as when inhomogeneous broadening dominates, recent studies show deviations that can become significant as sample quality improves or when laser behavior is examined in greater detail. These deviations originate from the carrier many-body interaction, involving the localized states, as well as the quasicontinuum of delocalized states, which reside in the wetting layer of self-assembled QD structures often used as laser gain media. In the screened Hartree-Fock approximation, the many-body interaction between localized and delocalized states can lead to substantial energy shift in the QD resonances and to nonvanishing carrier-induced refractive index change.[7] These predictions have been either directly or indirectly verified in experiments.[4,8]

A serious weakness of both atomlike and screened Hartree-Fock treatments is the phenomenological description of scattering effects with an effective relaxation rate approximation. Not only is predictive capability severely compromised by having the dephasing rate as a free parameter but experimental spectral shapes are not accurately reproduced. Furthermore, unlike the bulk and QW cases, there is an indication that the QD dephasing rate is strongly dependent on carrier density and possible electronic transitions. Consequently, the implementation of the effective relaxation rate description is not straightforward. To ensure accurate results, a microscopic gain theory with a rigorous treatment of carrier scattering processes should be used.

The dominant scattering processes in semiconductors arise from carrier-carrier and carrier-phonon interactions. They lead to the broadening and energy shift of the resonances due to dephasing and screening, respectively. When treated consistently, the broadening and energy shift are directly linked, as imaginary and real parts of the many-body self-energy. Typically, the determination of the self-energy uses perturbation theory that is based on the second Born approximation with strict energy conservation in terms of free-carrier states. While it gives satisfactory results for bulk and QW cases, there are indications that perturbation theory for QDs fails because of the discreteness of the localized states. For example, perturbation theory predicts a phonon bottleneck problem, whereas a more rigorous quantum-kinetic description in terms of renormalized quasiparticles (polarons)[9] correctly predicts efficient relaxation by carrier-phonon interaction under similar conditions.[10] The polaron treatment, together with a similar one for carrier-carrier scattering (with renormalized states), is incorporated into the laser theory used in our investigations.[11]

This letter begins with a description of the calculation procedure for QD gain and carrier-induced refractive change. Gain and refractive index spectra for two distinct QD configurations are computed for a range of carrier density. We extract the gain and carrier-induced refractive index change at the gain peaks as functions of carrier densities. Because these types of curves are used extensively in semiconductor laser simulations and because the results show functional differences from bulk or QW situations, we introduce new fitting functions for the QDs. These functions should facilitate the use of the microscopic results in laser models. Finally, we discuss the linewidth enhancement factor in QDs.

[a]Electronic mail: mlorke@itp.uni-bremen.de

The amplitude gain $g(\omega)$ and carrier-induced refractive index $\delta n(\omega)$ for a QW layer embedded with QDs are determined from the interband polarizations, $p_{ij}(\omega)$ and $p_{\mathbf{k}}(\omega)$,

$$K\delta n(\omega) + ig(\omega) = -\frac{\omega}{\varepsilon_0 n_B c w E(\omega)} \times \left[N_{\text{dot}} \sum_{i,j} \mu_{ij} p_{ij}(\omega) + \frac{1}{A} \sum_{\mathbf{k}} \mu_{\mathbf{k}} p_{\mathbf{k}}(\omega) \right], \quad (1)$$

where i and j label the QD states, $\mathbf{k}$ labels the QW states, c and ε_0 are the speed of light and permittivity in vacuum, n_B is the background refractive index, K is the laser field wavevector, w is the QW width, N_{dot} is the sheet density of QDs in a QW of area A, $E(\omega)$ is a weak laser probe field at frequency ω, and the summations are over all possible electron-hole transitions. For the polarization we solve the an equation of motion,

$$(\hbar\omega - \varepsilon_\alpha^e - \varepsilon_\alpha^h) p_\alpha + \hbar\Omega_\alpha (1 - n_\alpha^e - n_\alpha^h) = iS_\alpha^{c-c}(\omega) + iS_\alpha^{c-p}(\omega), \quad (2)$$

where $\hbar\Omega_\alpha$ and ε_α^β ($\beta = e, h$) are the renormalized Rabi energy and transition energy, n_α^β is the carrier population, and $S_\alpha^{c-c}(\omega)$ and $S_\alpha^{c-p}(\omega)$ are the complex carrier-carrier and carrier-phonon correlation (scattering) terms, respectively.[11,12] Equation (2) contains the free-carrier transition energies, the optical driving field, and the phase-space filling term with the population factors in a way that, restricted to these ingredients, a free-carrier theory for independent two-level systems would be obtained. The Coulomb interaction of carriers modifies this picture: the Hartree-Fock interaction terms lead to the coupling of QD and QW states, that describes excitonic effects as well as Hartree and exchange shifts of the single-particle energies. Furthermore, Coulomb correlation contributions contain the influence of screening, dephasing, and energy renormalization. A non-Markovian formulation with self-consistent renormalized states is used, and the interaction of carriers with LO phonons within the polaron picture is included. A typical calculation involves simultaneously solving around 100 coupled equations, each of the form given by Eq. (2). Details of the theory and numerics are described elsewhere.[11]

Calculations are performed for $In_{0.3}Ga_{0.7}As$ and InAs QDs. In each case, the QDs are embedded in GaAs QWs and the actual QD shape is approximated by a disk. For the $In_{0.3}Ga_{0.7}As$ QDs, a 2 nm height and 18 nm diameter are chosen to give a simple electronic structure, consisting of only one localized electronic state and one localized hole state. For the InAs QDs, the height and diameter of 3 and 20 nm, respectively, are chosen to obtain a ground-state emission wavelength at around 1.5 μm, which is interesting for optical fiber communication. The two structures enable us to examine the two very different scenarios of shallow and deep quantum confinements. Our investigation begins with calculating the gain and refractive index spectra for $T = 300$ K, QD density $N_{\text{dot}} = 5 \times 10^{10}$ cm^{-2}, and different carrier densities. The computed QD spectral resonances for both structures exhibit noticeable increase in linewidth with increasing carrier density, indicating strong dephasing rate dependence on excitation. Additionally, energy renormalizations give rise to redshifts of the QD resonances and refractive index spectra, not predicted by the atomlike theory.

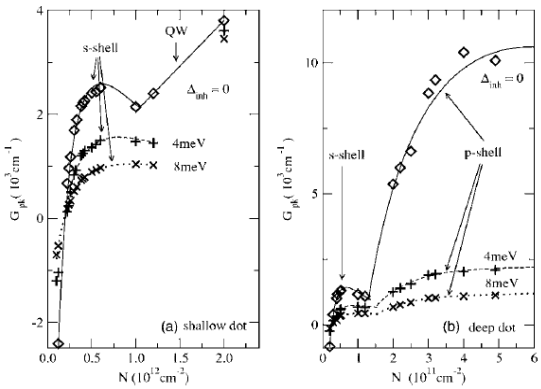

FIG. 1. Peak gain vs carrier density for different inhomogeneous broadenings. The symbols are the data from the calculations and the lines represent the fitting functions discussed in the text.

Many useful laser properties are determined by the excitation dependences of g and δn at the resonance peaks. Figures 1 and 2 show these dependences, where the points are extracted from the computed spectra and the curves are the least squares fit using fitting functions that we will discuss later. The inhomogeneously broadened results are obtained by performing a statistical average of the homogeneous spectra assuming an inhomogeneous width σ_{inh}. Contributions to inhomogeneous broadening may be from QD size or composition variations in a sample. The curves indicate significant saturation of the QD peak gain with increasing carrier density, even with $dG_{\text{pk}}/dN < 0$ in some cases. Gain saturation is of critical importance for laser applications because it limits the useful range of excitation densities. As in QW and bulk structures a contribution to gain saturation is the limitation of state filling according to the Pauli principle. However, for QDs, there is an additional contribution from the appreciable increase in the dephasing rate with excitation. The unique $dG_{\text{pk}}/dN < 0$ behavior at elevated carrier densities is a result of the dephasing increase overtaking the state-filling contribution.[13] Dephasing is also responsible for the difference in shallow and deep QD behaviors. Dephasing is weaker in the deep QD structure because of a scarcity of allowable scattering channels. As a result, the homogeneously broadened QD peak gain is con-

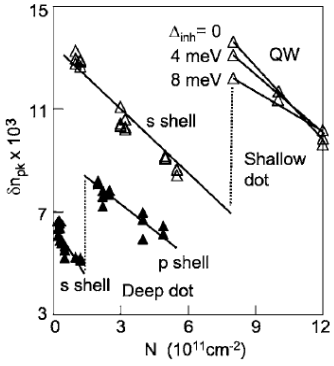

FIG. 2. Refractive index at the energetic position of the peak gain vs carrier density for deep and shallow dots and various inhomogenous broadenings.

TABLE I. Coefficients for QD gain and refractive index fitting functions.

	Shell	A	N_0	B	N_1
		(10^3/cm)	(10^{12}/cm^2)	(10^3/cm)	(10^{12}/cm^2)
			Shallow		
σ_{inh}=0	*s*	8.10	3.06	26.24	1.18
4 meV	*s*	2.95	3.36	9.61	1.58
8 meV	*s*	1.63	3.39	5.24	1.83
			Deep		
σ_{inh}=0	*s*	6.42	0.32	20.03	0.12
	p	14.35	30.40	83.05	2.78
4 meV	*s*	1.75	0.38	5.54	0.17
	p	4.70	1.02	12.33	0.62
8 meV	*s*	0.90	0.43	2.88	0.20
	p	2.74	0.92	7.01	0.55

	Shell	C (10^{-15} cm^2)	D
Shallow	*s*	−8.4	0.0135
Deep	*s*	−14	0.0065
	p	−7	0.0094

siderably higher and the spectral width is considerably narrower than in the case of the shallow QDs. The latter leads to greater sensitivity of the deep QDs to inhomogeneous broadening, as evidence by comparing Figs. 1(a) and 1(b). Figure 2 plots δn_{pk} at gain peak versus carrier density for both QD structures. Because of the symmetry in the δn_{pk} spectrum about the peak gain, δn_{pk} is insensitive to inhomogeneous broadening, as shown in Fig. 2, where the data points for the different inhomogeneous widths are basically inseparable. The data also indicate that δn_{pk} is to a good approximation linear in N.

Both g_{pk} vs N and δn_{pk} vs N curves are used extensively in semiconductor laser simulations. To facilitate the use of our results in laser models, we introduce the following fitting functions for the QDs:

$$G_{pk}(N) = A \ln(N/N_0) + B \exp(-N/N_1), \tag{3}$$

$$\delta n_{pk}(N) = CN + D, \tag{4}$$

where the first term in Eq. (3) is similar to the widely used QW gain fit function and we added the second term to account for the stronger saturation and possible gain reduction effects in QDs. Table I gives the coefficients used to obtain the curves in Fig. 1. These coefficients take into account the complicated dependences of scattering effects on carrier density and transition, as determined by the microscopic calculations.

The importance of δn is that its dependence on carrier density, relative to that of the gain, characterizes the QD contribution to laser linewidth, frequency chirp, and output beam quality. Specifically, $\alpha = -[Kd(\delta n)/dN] \times [dg/dN]^{-1}|_{\omega=\text{const}}$ defines both the linewidth enhancement factor and the antiguiding parameter. Figure 3 illustrates the dependence of α at the gain peak (where a laser typically operates) as a function of peak gain.

In the range of small peak gain our results show small values for the magnitude of α as expected for atomiclike systems. We find $|\alpha| \lesssim 1(2)$ with (without) inhomogeneous broadening. When gain saturation is approached (cf. Fig. 1) the denominator in the definition of the α factor approaches zero and, hence, the magnitude of the α factor increases drastically. The sign of the α factor is determined by the

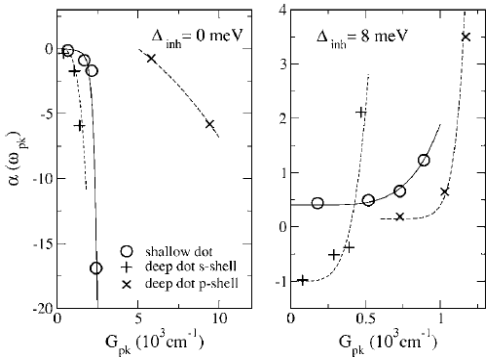

FIG. 3. α factor vs peak gain for deep and shallow dot: (a) without inhomogeneous broadening and (b) with inhomogeneous broadening of 8 meV. The lines are guides for the eye.

behavior of the index change at constant energy, and this behavior changes due to the flattening of the index curves in the presence of inhomogeneous broadening. Please note that Fig. 2 displays the index at the peak gain and that the slope of these curves is different from the variation of the index at *fixed energy* for a small density variation. For the deep dot, the divergence of α_{pk} may be delayed by operating with the *p*-shell transition, as indicated in Fig. 3.

In summary, this letter explores the excitation dependences of quantum-dot gain and carrier-induced refractive-index change. The behaviors in the vicinity of the gain peak are important for understanding laser threshold, noise, and modulation response characteristics, in addition to being necessary as input to quantum-dot laser models. A microscopic theory with a quantum-kinetic treatment of scattering is necessary because little is known quantitatively about the dephasing rate. The theory also uncovers the complicated carrier density and electronic structure influences on quantum-dot dephasing, which in turn determines the excitation dependences of gain and refractive indices.

The work is supported by the U. S. Department of Energy under Contract No. DE-AC04-94AL85000, the Deutsche Forschungsgemeinschaft, NIC of Forschungszentrum Jülich, and the Humboldt Foundation.

[1]For a text book discussion, see D. Bimberg, M. Grundmann, and N. N. Ledentsov, *Quantum Dot Heterostructures* (Wiley, New York, 1999).
[2]J. Tatebayashi, N. Hatori, and Y. Aarakawa, Electron. Lett. **39**, 1130 (2003).
[3]S. Deubert, R. Debusmann, J. P. Reithmaier, and A. Forchel, Electron. Lett. **41**, 1125 (2005).
[4]P. M. Smowton, E. J. Pearce, H. C. Schneider, W. W. Chow, and M. Hopkinson, Appl. Phys. Lett. **81**, 3251 (2002).
[5]D. Bimberg, J. Phys. D **38**, 2055 (2005).
[6]S. Fathpour and P. Bhattacharya, J. Phys. D **38**, 2103 (2005).
[7]H. C. Schneider, W. W. Chow, and S. W. Koch, Phys. Rev. B **64**, 115315 (2001).
[8]K. Matsuda, K. Ikeda, T. Saiki, H. Saito, and K. Nishi, Appl. Phys. Lett. **83**, 2250 (2003).
[9]T. Inoshita and H. Sakaki, Phys. Rev. B **56**, R4355 (1997).
[10]J. Seebeck, T. R. Nielsen, P. Gartner, and F. Jahnke, Phys. Rev. B **71**, 125327 (2005).
[11]M. Lorke, T. R. Nielsen, J. Seebeck, P. Gartner, and F. Jahnke, Phys. Rev. B **73**, 085324 (2006).
[12]H. C. Schneider, W. W. Chow, and S. W. Koch, Phys. Rev. B **70**, 235308 (2004).
[13]M. Lorke, W. W. Chow, T. R. Nielsen, J. Seebeck, P. Gartner, and F. Jahnke, Phys. Rev. B **74**, 035334 (2006).

Journal of Modern Optics
Vol. 54, Nos. 16–17, 10–20 November 2007, 2413–2424

Taylor & Francis
Taylor & Francis Group

Many-body theory of quantum coherence in semiconductor quantum dots

W. W. CHOW*†, S. MICHAEL‡ and H. C. SCHNEIDER‡
†Sandia National Laboratories, Albuquerque, NM 87185-1086, USA
‡Physics Department, Kaiserslautern University, 67653 Kaiserslautern, Germany

(*Received 27 March 2007; in final form 14 August 2007*)

A many-body theory for quantum coherence in a semiconductor quantum-dot system is presented. We present the theory in detail for a Λ scheme in a InGaAs–GaAs quantum dot with a pulsed drive field. The paper shows the significant differences in the predictions of this theory and those of an independent-particle treatment, adapted from atomic quantum coherence theory. Specifically, the influence of the quantum-dot level structure on group-velocity slowdown is discussed, and the influence of different Coulomb renormalization effects is analysed.

1. Introduction

Success in demonstrating quantum coherence phenomena in atomic systems [1–3] has created interest in achieving similar results in semiconductors. Both physics and device engineering issues are currently explored for different condensed-matter systems [4–9]. Some recent work has been directed towards semiconductor quantum dots (QDs) [10, 11] because of reports of long dephasing times [12] and promising atomic-like properties (e.g. discrete energy levels) of QDs at high temperatures. For instance, optical buffers using slow light and EIT in QDs have been proposed and analysed [10].

To date, the majority of the theoretical analyses of quantum-coherence effects in QDs are based on atomic quantum-coherence theory [10, 13]. They do not contain a complete description of semiconductor behaviour because many-body effects due to the Coulomb interaction between charged carriers are neglected [11, 14]. In this paper, we show in detail how one can include these interaction effects in a straightforward manner to model quantum-coherence phenomena in realistic QDs, and present some applications of the theory, which illustrate that many-body effects can give rise to significant differences from atomic theory. In section 2 we describe the general theoretical formulation. The many-body contributions are especially highlighted to show the deviation from conventional quantum-coherence theory.

*Corresponding author. Email: wwchow@sandia.gov

Journal of Modern Optics
ISSN 0950–0340 print/ISSN 1362–3044 online © 2007 Taylor & Francis
http://www.tandf.co.uk/journals
DOI: 10.1080/09500340701639664

In section 3, the theory is applied to treat the case of a pulse driven Λ configuration in an InGaAs–GaAs QD structure. The role of the combined influence of many-body contributions and the QD level structure on the optical response is stressed. Also, numerical results are presented for the influence of many-body Coulomb renormalizations and collisions on the slowdown factor, which characterizes the maximum achievable group-velocity reduction.

2. Theory

The derivation of the semiconductor medium equations is based on the many-body Hamiltonian for interacting electrons and holes in the quantum-dot material under the influence of an external field:

$$H = \sum_n \varepsilon_n a_n^\dagger a_n + \sum_m \varepsilon_m b_m^\dagger b_m - \sum_{n,m} \left(\mu_{nm} a_n^\dagger b_m^\dagger + \mu_{nm}^* b_m a_n\right) E(z,t) + \frac{1}{2} \sum_{n,m,r,s} V_{nm}^{rs} a_r^\dagger a_s^\dagger a_m a_n + \frac{1}{2} \sum_{n,m,r,s} V_{nm}^{rs} b_r^\dagger b_s^\dagger b_m b_n - \sum_{n,m,r,s} V_{nm}^{rs} a_r^\dagger b_s^\dagger b_m a_n. \quad (1)$$

The first three terms describe independent particles interacting with an external field, and are the basis of an atomic-like description of QDs. They describe the kinetic energies of the noninteracting electrons and holes (ε_n is the free-carrier electron or hole energy), and the dipole interaction (μ_{nm} is the dipole matrix element) of electron–hole pairs with the optical field, $E(z,t)$. To include many-body effects, we add to the independent-particle Hamiltonian the contributions from electron–electron and hole–hole Coulomb repulsion and the electron–hole Coulomb attraction (the last three terms). These terms contain matrix elements of the Coulomb interaction energy

$$V_{nm}^{rs} = \int \mathrm{d}^3 r \, \mathrm{d}^3 r' \, \phi_r^*(\mathbf{r}) \phi_s^*(\mathbf{r}') \frac{e^2}{4\pi\varepsilon_b |\mathbf{r} - \mathbf{r}'|} \phi_m(\mathbf{r}') \phi_n(\mathbf{r}), \quad (2)$$

where e is the electron charge, ε_b is the host permittivity and ϕ_n is a wavefunction of a localized QD state or of a delocalized (scattering) state in the quantum well, in which the QDs are embedded. In equation (1), a_n and $a_n^\dagger$ are electron annihilation and creation operators, b_m and $b_m^\dagger$ are the corresponding operators for holes. Again, the subscripts and superscripts refer in general to either localized QD states or delocalized quantum-well states. For a quantum coherence configuration, the optical field is

$$E(z,t) = \frac{1}{2}\Big[E_\mathrm{d}(t) \exp(\mathrm{i}k_\mathrm{d} z - \mathrm{i}\omega_\mathrm{d} t) + E_\mathrm{p}(t) \exp(\mathrm{i}k_\mathrm{p} z - \mathrm{i}\omega_\mathrm{p} t) + E_\mathrm{d}(t) \exp(-\mathrm{i}k_\mathrm{d} z + \mathrm{i}\omega_\mathrm{d} t) + E_\mathrm{p}^*(t) \exp(-\mathrm{i}k_\mathrm{p} z + \mathrm{i}\omega_\mathrm{p} t) \Big], \quad (3)$$

where z is position along the propagation direction, k_j is the wavevector, ω_j is the frequency, the subscripts 'd' and 'p' identify the drive and probe fields, and the slowly

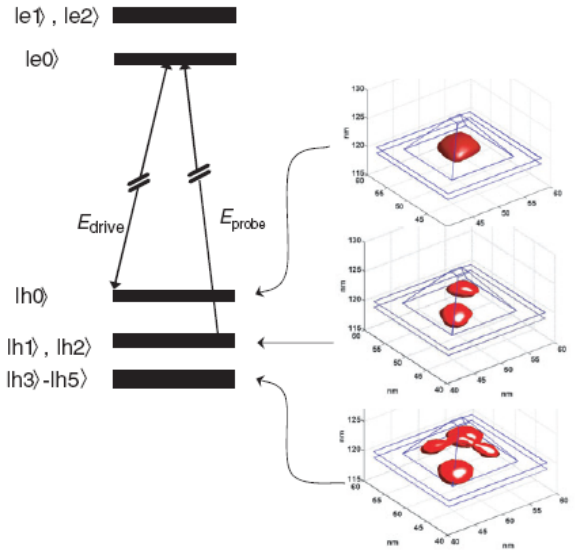

Figure 1. Electronic level structure for InAs quantum dot structure used in the quantum-coherence calculations. The shape of the pyramidal QD and contour plots (30%) of the absolute squares of the envelope wavefunctions are shown on the right. The arrows indicate the optical transitions of the Λ scheme. (The colour version of this figure is included in the online version of the journal.)

varying probe field amplitude E_p is complex to allow for a phase difference between it and the (real) drive field amplitude E_d.

The equations of motion for the polarizations and populations are derived in the Heisenberg picture. Because of the Coulomb interaction terms in equation (1), the result is an infinite hierarchy of coupled differential equations. Each level of the hierarchy describes a higher order correlation effect in the Coulomb potential than the one before. At the first level are the Hartree–Fock contributions, which give rise to band gap renormalization and Coulomb enhancement of the optical transitions. Scattering and dephasing contributions appear in the next higher level in the equation hierarchy. The present approach to describe quantum coherence effects in QDs truncates the hierarchy to include only the Hartree–Fock contributions and includes dephasing and scattering contributions at the level of a relaxation-time approximation.

To facilitate the presentation of the resulting equations of motion, we choose a specific experimental structure, consisting of InAs QDs embedded in a GaAs quantum well. Figure 1 depicts the computed electronic levels, assuming pyramidal dots, each with a base of 12×12 nm and height 6 nm, and an InAs wetting layer of thickness 1 nm. Using the input material parameters listed in table 1, the numerical calculation using a software package [15] adapted for our purposes gives three confined electron and six confined hole levels, which are spin degenerate. It also produces the envelope wavefunctions, which are shown schematically in figure 1 using contour plots of their absolute squares. The envelope wavefunctions are used to determine dipole and Coulomb matrix elements in equation (2). The level

Table 1. Numerical parameters used in the calculation of QD wave functions and energies using the software package *nextnano*[3] [15, 16]. Here m_0 is the vacuum electron mass.

Quantity	Symbol/unit	Numerical value for $In_xGa_{1-x}As$
Bandgap	E_0/meV	$1518 - 1580x + 475x^2$
Spin–orbit coupling	Δ_0/meV	$340 - 93x + 133x^2$
Optical matrix parameter	E_p/meV	$(1.238 - 0.2095x)\dfrac{1 - m_e}{m_e}\dfrac{3E_0(E_0 + \Delta_0)}{3E_0 + 2\Delta_0}$
CB effective mass	m_e/m_0	$0.0667 - 0.0419x - 0.00254x^2$
Luttinger parameter	γ_1	$(1 - x)7.1 + x19.7$
Luttinger parameter	γ_2	$(1 - x)2.02 + x8.4$
Luttinger parameter	γ_3	$(1 - x)2.91 + x9.3$

energies and dipole transition selection rules give rise to a slightly modified Λ configuration, with the drive field connecting the $|e0\rangle$ and $|h0\rangle$ states, and a probe field close to resonance to the transitions $|e0\rangle \rightarrow |h1\rangle$, as well as $|e0\rangle \rightarrow |h2\rangle$ (see figure 1). The other QD and quantum well states in figure 1 are coupled to one another and to the states in the Λ configuration via collisions.

For the above experimental situation, the following equations-of-motion result for the polarizations $p_{\alpha\beta}$ between QD electron state α and hole state β are

$$\frac{\partial}{\partial t}p_{e_0h_0} = -(\mathrm{i}\omega_{e_0h_0} + \gamma_\mathrm{d})p_{e_0h_0} - \mathrm{i}\Omega_{e_0h_0}\left(n_{e_0} + n_{h_0} - 1\right) + \mathrm{i}\sum_{\beta\neq h_0}{}'\Omega_{e_0\beta}p_{h_0\beta} - \mathrm{i}\sum_{\beta\neq h_0}{}'\mathrm{i}\Delta\Omega_{\beta h_0}p_{\beta e_0}, \tag{4}$$

$$\frac{\partial}{\partial t}p_{e_0h_1} = -(\mathrm{i}\omega_{e_0h_1} + \gamma_\mathrm{d})p_{e_0h_1} - \mathrm{i}\Omega_{e_0h_1}\left(n_{e_0} + n_{h_1} - 1\right) + \mathrm{i}\sum_{\beta\neq h_1}{}'\Omega_{e_0\beta}p_{h_1\beta} - \mathrm{i}\sum_{\beta\neq h_1}{}'\Delta\Omega_{\beta h_1}p_{\beta e_0}, \tag{5}$$

$$\frac{\partial}{\partial t}p_{e_0h_2} = -(\mathrm{i}\omega_{e_0h_2} + \gamma_\mathrm{d})p_{e_0h_2} - \mathrm{i}\Omega_{e_0h_2}\left(n_{e_0} + n_{h_2} - 1\right) + \mathrm{i}\sum_{\beta\neq h_2}{}'\Omega_{e_0\beta}p_{h_2\beta} - \mathrm{i}\sum_{\beta\neq h_2}{}'\Delta\Omega_{\beta h_2}p_{\beta e_0}. \tag{6}$$

For the time development of the electron and hole populations, n_α and n_β, one obtains

$$\frac{\partial}{\partial t}n_{e_0} = \mathrm{i}\sum_{\beta}{}'\left(\Omega_{e_0\beta}p^*_{e_0\beta} - \Omega^*_{e_0\beta}p_{e_0\beta}\right) - \gamma^\mathrm{d}_\mathrm{nr}n_{e0} - \gamma^\mathrm{d}_{\mathrm{c-c}}\left[n_{e0} - f_{e0}\left(\mu^\mathrm{p}_e, T_\mathrm{p}\right)\right] - \gamma^\mathrm{d}_{\mathrm{c-p}}\left[n_{e0} - f_{e0}\left(\mu^\mathrm{l}_e, T_\mathrm{l}\right)\right], \tag{7}$$

$$\frac{\partial}{\partial t}n_{h_0} = \mathrm{i}\left(\Omega^*_{e_0h_0}p_{e_0h_0} - \Omega_{e_0h_0}p^*_{e_0h_0}\right) - \gamma^\mathrm{d}_\mathrm{nr}n_{h0} - \gamma^\mathrm{d}_{\mathrm{c-c}}\left[n_{h0} - f_{h0}\left(\mu^\mathrm{p}_h, T_\mathrm{p}\right)\right] - \gamma^\mathrm{d}_{\mathrm{c-p}}\left[n_{h0} - f_{h0}\left(\mu^\mathrm{l}_h, T_\mathrm{l}\right)\right], \tag{8}$$

$$\frac{\partial}{\partial t}n_{h_1} = \mathrm{i}\left(\Omega^*_{e_0h_1}p_{e_0h_1} - \Omega_{e_0h_1}p^*_{e_0h_1}\right) - \gamma^{\mathrm{d}}_{\mathrm{nr}}n_{h1} - \gamma^{\mathrm{d}}_{\mathrm{c-c}}\left[n_{h1} - f_{h1}\left(\mu^{\mathrm{p}}_h, T_{\mathrm{p}}\right)\right] - \gamma^{\mathrm{d}}_{\mathrm{c-p}}\left[n_{h1} - f_{h1}\left(\mu^{\mathrm{l}}_h, T_{\mathrm{l}}\right)\right], \tag{9}$$

$$\frac{\partial}{\partial t}n_{h_2} = \mathrm{i}\left(\Omega^*_{e_0h_2}p_{e_0h_2} - \Omega_{e_0h_2}p^*_{e_0h_2}\right) - \gamma^{\mathrm{d}}_{\mathrm{nr}}n_{h1} - \gamma^{\mathrm{d}}_{\mathrm{c-c}}\left[n_{h2} - f_{h2}\left(\mu^{\mathrm{p}}_h, T_{\mathrm{p}}\right)\right] - \gamma^{\mathrm{d}}_{\mathrm{c-p}}\left[n_{h2} - f_{h2}\left(\mu^{\mathrm{l}}_h, T_{\mathrm{l}}\right)\right], \tag{10}$$

$$\frac{\partial}{\partial t}n_{e_n} = -\gamma^{\mathrm{d}}_{\mathrm{nr}}n_{en} - \gamma^{\mathrm{d}}_{\mathrm{c-c}}\left[n_{e_n} - f_{e_n}\left(\mu^{\mathrm{p}}_e, T_{\mathrm{p}}\right)\right] - \gamma^{\mathrm{d}}_{\mathrm{c-p}}\left[n_{e_n} - f_{e_n}\left(\mu^{\mathrm{l}}_e, T_{\mathrm{l}}\right)\right], \tag{11}$$

$$\frac{\partial}{\partial t}n_{h_n} = -\gamma^{\mathrm{d}}_{\mathrm{nr}}n_{hn} - \gamma^{\mathrm{d}}_{\mathrm{c-c}}\left[n_{h_n} - f_{h_n}\left(\mu^{\mathrm{p}}_h, T_{\mathrm{p}}\right)\right] - \gamma^{\mathrm{d}}_{\mathrm{c-p}}\left[n_{h_n} - f_{h_n}\left(\mu^{\mathrm{l}}_h, T_{\mathrm{l}}\right)\right].$$

In the above equations, γ^{d} is the dephasing rate, $\gamma^{\mathrm{d}}_{\mathrm{nr}}$, $\gamma^{\mathrm{d}}_{\mathrm{c-c}}$ and $\gamma^{\mathrm{d}}_{\mathrm{c-p}}$ are effective nonradiative recombination, carrier–carrier scattering, and carrier–phonon scattering rates, respectively. Primed sums indicate that the summations run over electron and/or hole states that are connected by polarizations close to resonance with the drive and probe fields. The labels e_n and h_n stand for electron and hole states that do not belong to the Λ configuration as shown in figure 1.

One difference to the corresponding atomic equations involves the transition and Rabi frequencies $\omega_{\alpha,\beta}$ and $\Omega_{\alpha,\beta}$, respectively, which are renormalized by excitation-dependent many-body Coulomb interaction contributions:

$$\omega_{\alpha\beta} = \omega^{(0)}_{\alpha\beta} + \left(\Delta^{\mathrm{d}}_{\beta,\beta} + \Delta^{\mathrm{d}}_{\alpha}\right), \tag{12}$$

$$\Omega_{\alpha\beta} = \mu_{\alpha,\beta}(E_{\mathrm{p}} + E_{\mathrm{d}}) + \Delta^{\mathrm{nd}}_{\alpha,\beta}, \tag{13}$$

$$\Delta\Omega_{\beta^0\beta} = \Delta^{\mathrm{d}}_{\beta^0,\beta}, \tag{14}$$

where $\omega^{(0)}_{\alpha,\beta}$ and $\mu_{\alpha,\beta}$ are the transition frequency and dipole matrix element determined from the single-particle electronic-structure calculation. The many-body renormalizations in the Hartree–Fock approximation may be grouped into terms that are nondiagonal (nd), i.e.,

$$\hbar\Delta^{\mathrm{nd}}_{\alpha,\beta} = {\sum_{\alpha'\beta'}}' V^{\alpha\beta}_{\alpha'\beta'}p_{\beta'\alpha'} \tag{15}$$

and contributions that are diagonal (d),

$$\hbar\Delta^{\mathrm{d}}_{\beta^0,\beta} = -\sum_{\beta'}\left(V^{\beta^0\beta}_{\beta'\beta'} - V^{\beta^0\beta'}_{\beta\beta'}\right)n_{\beta'} - \sum_{\alpha'}V^{\beta^0\alpha'}_{\beta\alpha'}n_{\alpha'} - \sum_{k}V^{\beta^0\beta}_{kk}n^h_k + {\sum_{\beta',\beta''\neq\beta'}}'\left(V^{\beta^0\beta}_{\beta''\beta'} - V^{\beta^0\beta'}_{\beta\beta''}\right)p_{\beta'\beta''}, \tag{16}$$

$$\hbar\Delta^{\mathrm{d}}_{\alpha} = -\sum_{\alpha'}\left(V^{\alpha\alpha}_{\alpha'\alpha'} - V^{\alpha\alpha'}_{\alpha\alpha'}\right)n_{\alpha'} - \sum_{\beta'}V^{\alpha\beta'}_{\alpha\beta'}n_{\beta'} - \sum_{k}V^{\alpha\alpha}_{kk}n^e_k + {\sum_{\beta',\beta''\neq\beta'}}'V^{\alpha\beta'}_{\alpha\beta''}p_{\beta'\beta''}. \tag{17}$$

For a discussion on the separation into diagonal and nondiagonal contributions, see [17]. The summations are over QD levels with α standing for electron and β for hole indices, and k for quantum well states. Each term on the right-hand side contains matrix elements of the Coulomb interaction energy defined in equation (2).

In a screened Hartree–Fock treatment, the screening effects are for the present situation assumed to arise from the changes in the dielectric function due to the presence of carriers in the quantum well states [18]. For the present InAs QDs, the quantum well carrier population is negligible because of the relatively deep InAs QD confinement, and the plasma screening contributions are neglected. We do not take into account microscopic dephasing processes that couple the polarization of interest to other polarizations and thus give rise to diagonal and nondiagonal scattering contributions [19]. We account for these contributions in equations (4)–(6) by an effective dephasing rate γ^{d}.

Besides the Hartree–Fock contributions, the population and therefore the polarization dynamics between semiconductors and atomic systems differ due to population relaxation. For the quantum-coherence dynamics in a QD, we use a relaxation-time approximation for the interaction-induced carrier–carrier and carrier–phonon scattering processes that drive the electron and hole populations to quasiequilibrium Fermi–Dirac distributions f_α and f_β, respectively, at chemical potentials and temperatures $(\mu^{\mathrm{p}}_{e/h}, T_{\mathrm{p}})$ and $(\mu^{\mathrm{l}}_{e/h}, T_{\mathrm{l}})$, where T_{p} and T_{l} are the plasma and lattice temperatures, respectively. These relaxation processes couple the four QD states, that participate directly in the quantum-coherence process, to the other states of the system. The chemical potentials and temperatures are determined using total density conservation in carrier–carrier and carrier–phonon collisions, together with total energy conservation in carrier–carrier collisions. The details are given in [11].

3. Results

Self-organized QDs based on the InAs–GaAs material system usually grow in pyramidal structures, which set up strain and piezoelectric fields that influence the structure of the electronic levels in the QDs and the form of the corresponding wavefunction. The resulting electron and hole level schemes typically do not show exact degeneracies that rotationally symmetric QD models with effective-mass approximation have, which is often assumed in theoretical treatments to keep the determination of the single-particle states simpler. A more realistic multiband calculation for pyramidal structures including the combined effects of three-dimensional confinement, strain, and piezoelectric fields leads to a level scheme for the InAs QD considered here, in which the excited electron and hole states are still energetically close together (see figure 1) but not degenerate, which would be the case in a rotationally symmetric structure. Due to the lack of symmetry of realistic QD structures, energetically close excited states are present in a variety of QD systems, and the structure of the QD level scheme should also be taken into account when considering quantum-coherence effects in QDs. In the following, we first discuss the overall shape of the optical response including quantum-coherence effects and the influence of Coulomb renormalizations at the Hartree–Fock level and population scattering. We then focus on the contributions to the spectrum that arise due to different electron–hole transitions and show how these different contributions affect the overall optical response in our quantum-coherence scheme.

We present results obtained from numerically solving the equations of motion for the case where an optical pulse is incident on the InAs QD sample to drive the polarization $p_{e0,h0}$, and a continuous-wave probe field is used to examine the complex susceptibility arising from the polarizations $p_{e0,h1}$ and $p_{e0,h2}$. Both fields are σ^+ polarized and propagate in the z direction, i.e. perpendicularly to the two-dimensional arrangement of QDs. The calculations are performed for a dot density of $N_\mathrm{d} = 5 \times 10^{10}\,\mathrm{cm}^{-2}$ and lattice temperature $T_\mathrm{l} = 200\,\mathrm{K}$, where recent literature [20] gives scattering rates around $\gamma^\mathrm{d} = 1.5 \times 10^{12}\,\mathrm{s}^{-1}$, $\gamma_{\mathrm{c-c}} = 2 \times 10^{12}\,\mathrm{s}^{-1}$ and $\gamma_{\mathrm{c-p}} = 2 \times 10^{11}\,\mathrm{s}^{-1}$.

From the microscopic polarizations the macroscopic polarization is calculated according to

$$P(t) = \frac{2N_\mathrm{d}}{L} \sum_{\alpha\beta} \mu_{\alpha\beta} p_{\alpha\beta}(t), \tag{18}$$

where L is the thickness of the quantum well, in which the QDs are imbedded, and P and μ are the components of $\mathbf{P}$ and $\boldsymbol{\mu}$ for the field polarization. In the presence of the time-dependent drive field $E_\mathrm{d}(t)$, we calculate the transient quantities that describe gain

$$g(\omega_\mathrm{p}) = -\frac{\omega_\mathrm{p}}{2\varepsilon_0 c_0 n_\mathrm{b} E_\mathrm{p}} \operatorname{Im} P \tag{19}$$

and refractive-index change

$$\delta n(\omega_\mathrm{p}) = \frac{1}{2\varepsilon_0 n_\mathrm{b} E_\mathrm{p}} \operatorname{Re} P \tag{20}$$

experienced by the weak CW probe field with a fixed frequency ω_p and field strength E_p. We also average over the phase of the probe field. Here, n_b is the background refractive index of the host material, and c_0 is the vacuum speed of light. Figure 2 shows the transient gain, defined in equation (19), as a function of probe frequency for three different times: before the pulse, at the time of maximum transient amplification and after the pulse. To illustrate the contributions from many-body effects, the results presented in the left column are obtained using the many-body treatment described above, i.e. including Coulomb renormalizations of transition and Rabi energies together with population scattering. The results in the right column are obtained using an independent-particle approximation, in which energy renormalizations, Coulomb enhancement and scattering contributions are neglected. To facilitate comparison of the shapes of the spectra in both cases, the results in the left column for the interacting case are plotted with a shift of $\varepsilon_x \equiv V^{e_0 h_2}_{e_0 h_2}$, which is a Rabi-energy renormalization, via equations (15) and (13), to the equation of motion (6). This particular term is proportional to $p_{e0,h2}$ and corresponds to the Coulomb binding energy of an electron–hole pair (or exciton) in states $|e0\rangle$ and $|h2\rangle$, respectively. The series of snapshots is obtained using a sech drive pulse with peak intensity $2\,\mathrm{MW\,cm}^{-2}$ for the simulation including Coulomb interaction, and $21.9\,\mathrm{MW\,cm}^{-2}$ for the independent-particle calculation. The duration (FWHM) of the drive pulse is 1.7 ps in both cases, and the intensities are chosen so that in both cases the probe absorption after the pump pulse is comparable. The solid lines show

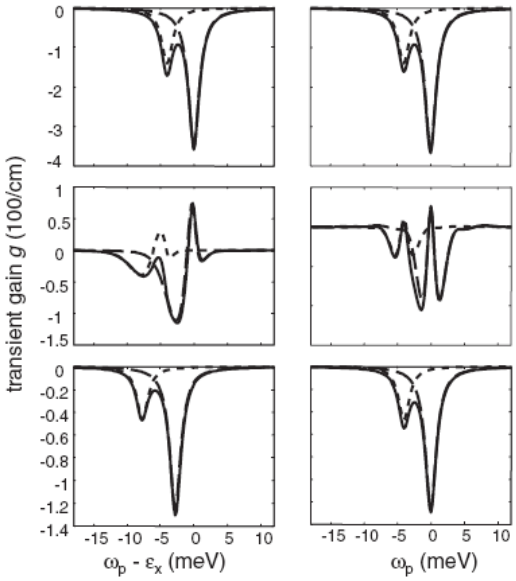

Figure 2. Spectra of the transient gain experienced by the probe field at different times. Top row: before the drive pulse, middle row: during the drive pulse (0.2 ps after the drive-pulse maximum), and bottom row: after the drive pulse. The spectra are obtained including Coulomb effects (left column) and using the independent particle model (right column). The solid line is the result if all relevant transitions in the QD are included, the dotted line and dashed lines correspond to including, respectively, only the $|e0\rangle \rightarrow |h1\rangle$ and $|e0\rangle \rightarrow |h2\rangle$ transitions in the calculation. ε_x is the (excitonic) interaction energy of an electron and hole in states $|e0\rangle$ and $|h2\rangle$, respectively, which is subtracted to facilitate the comparison of the optical response with that of the independent-particle model.

the resulting spectra including the transitions $|e0\rangle \rightarrow |h1\rangle$ and $|e0\rangle \rightarrow |h2\rangle$ relevant for the interaction with the probe field in our quantum-coherence scheme. The dotted and dashed lines are the results if the calculations are done including only one of the transitions $|e0\rangle \rightarrow |h1\rangle$ and $|e0\rangle \rightarrow |h2\rangle$, respectively.

Prior to the drive pulse and after the drive pulse (top and bottom graphs in figure 2), the absorption profiles with and without Coulomb interaction are comparable. During the action of the drive pulse (the snapshot is 0.2 ps after the drive-pulse maximum and corresponds to the maximum transient gain achieved), the spectral bandwidth is approximately the same, but the shape of the transient absorption spectrum with and without Coulomb interaction is different, and these differences can be exhibited more clearly by looking at the contributions from the two transitions $|e0\rangle \rightarrow |h1\rangle$ and $|e0\rangle \rightarrow |h2\rangle$: in the independent-particle model, the contributions from both transitions are symmetric around the individual resonance energies, but each of these contributions acquires a distinct asymmetry if Coulomb effects are taken into account. More specifically, the absorption at the respective resonances and on the high energy side of each of the resonances is decreased, whereas on the low energy side of the resonance the transient absorption is increased mainly due to the dynamical Coulomb renormalizations. Also note that

the individual resonances undergo time-dependent excitation-induced shifts to lower energy. The asymmetry along with the frequency dependent decrease in absorption or, equivalently, the increase in transient gain at the individual resonances leads to transient gain on the $|e0\rangle \rightarrow |h2\rangle$ transition at a pump intensity that is much lower than what is needed to achieve a similar transient gain in the independent-particle case. However, the pronounced asymmetry in the contributions from the individual transitions is the reason that only the transient gain due to the $|e0\rangle \rightarrow |h2\rangle$ transition survives in the actual QD spectrum. While the contribution from $|e0\rangle \rightarrow |h1\rangle$ alone reaches transient gain, this is cancelled by the absorption from the $|e0\rangle \rightarrow |h2\rangle$ transition. In the independent-particle calculation, on the other hand, no such cancellation effect occurs because the higher drive intensity necessary to reach transient amplification leads to sharper individual resonances. Hence, the contributions from both transitions show up as distinct transient gain maxima.

Oftentimes one is not only interested in the occurrence of transient excitation-induced transparency or gain, but the group velocity slowdown that can be achieved over a frequency bandwidth near transparency or amplification. A measure of the group-velocity slowdown due to excitation-induced refractive-index changes is the slow-down factor,

$$S(\omega_{\mathrm{p}}) = n_b + \omega_{\mathrm{p}} \frac{\mathrm{d}(\delta n)}{\mathrm{d}\omega_{\mathrm{p}}}, \tag{21}$$

where δn is the transient excitation-induced refractive index change. Figure 3 shows the corresponding differences in the frequency dependent contribution to the slow-down factor, $\omega_{\mathrm{p}}\mathrm{d}(\delta n)/\mathrm{d}\omega_{\mathrm{p}}$, resulting from the present theory and the independent-particle treatment. Comparison of the results indicates that appreciable differences can occur between the two descriptions. Again, the Coulomb renormalizations give rise to asymmetries in the resonances and different spectral peak amplitudes [11].

From the discussion of the transient amplification above one would expect that there may be similar cancellation effects for the contributions of the two individual resonances to the slowdown factor. However, this is not the case: the spectral contributions from the transitions $|e0\rangle \rightarrow |h1\rangle$ and $|e0\rangle \rightarrow |h2\rangle$ to S are narrower than their counterparts in the transient absorption spectra. In the independent-particle model the contributions of the individual transitions to S do not overlap either, as in the case of the corresponding transient gain spectra. Due to the higher drive intensity, the independent particle model therefore, yields group-velocity slowdown together with transparency/gain over a wider bandwidth. Including Coulomb interactions, however, leads to a drastically reduced drive field intensity and thus to group-velocity slowdown including transparency/gain over a smaller bandwidth.

Since the spectral properties of the gain and slowdown are complicated, we concentrate in the following on the maximum achievable slowdown, which we extract for a range of drive intensities I_{d} by analysing spectra similar to those in figure 3. The result is plotted in figure 4 for the independent-particle model (dotted line) and including Coulomb renormalizations (solid line).

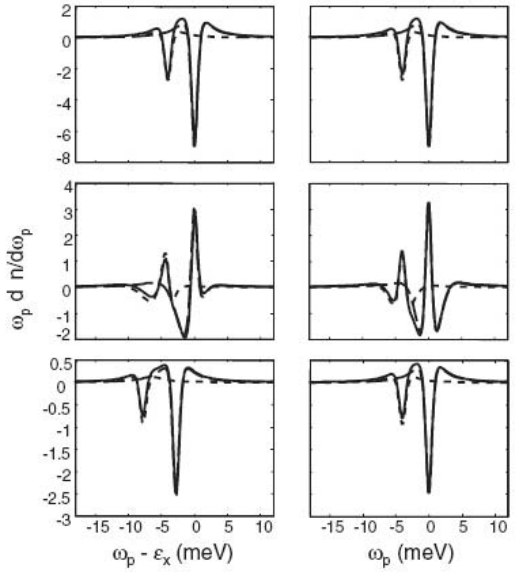

Figure 3. Frequency dependent contribution to the slowdown factor, $\omega_p d\delta n/d\omega_p$ experienced by the probe field at different times. Top row: before the drive pulse, middle row: during the drive pulse (0.2 ps after the drive-pulse maximum), and bottom row: after the drive pulse. The spectra are obtained including Coulomb effects (left column) and using the independent particle model (right column). The solid line is the result if all relevant transitions in the QD are included, the dotted line and dashed lines correspond to including, respectively, only the $|e0\rangle \rightarrow |h1\rangle$ and $|e0\rangle \rightarrow |h2\rangle$ transitions in the calculation. ε_x is the (excitonic) interaction energy of an electron and hole in states $|e0\rangle$ and $|h2\rangle$, respectively, which is subtracted to facilitate the comparison of the optical response with that of the independent-particle model.

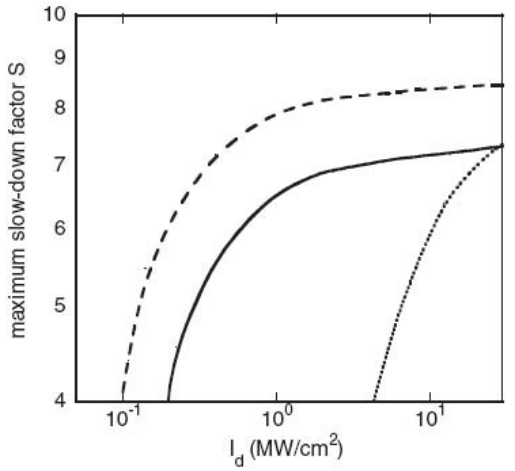

Figure 4. Maximum slowdown factor S_{max} experienced by the probe pulse *versus* drive pulse peak intensity for different model calculations. The solid and dotted curves are the many-body and independent-particle results, respectively. The dashed curve results if the Rabi-energy renormalizations are turned off in the numerical calculation.

Again, comparison of solid and dashed curves shows the significance of many-body contributions because neglecting them leads to over two orders of magnitude overestimation of the necessary drive pulse intensity to reach a given group-velocity slowdown. On the other hand, both treatments predict basically the same maximum achievable slow-down even though the drive intensities for reaching saturation is drastically different. We also investigate here the relative influence of the renormalization of the transition energies, cf. equation (12), and the Rabi energies, cf. equations (13) and (14). The dashed line shows a calculation for the artificial case, in which all the Rabi energy renormalizations are neglected. In this case, the drive intensity requirement is actually lower than the one obtained by including all Coulomb renormalizations, but the influence of the Rabi-energy renormalization on the dependence on the drive intensity is smaller than the transition energy renormalizations. This is in contrast to our earlier investigations of InGaN-based QDs [11], where we found that the Rabi-energy enhancement played a more important role for the Coulomb effects on the group-velocity reduction than the transition-energy renormalizations. The reason for the different behaviours is that, in confined systems, the performance of quantum-coherence schemes depends on the dipole-matrix elements and the Coulomb matrix elements coupling the individual localized levels, and it is possible to have a competition between the different Coulomb renormalization terms. This result points to the importance of the electronic structure for the calculation of Coulomb effects in quantum-coherence schemes in QDs.

4. Conclusions

In conclusion, we showed that the incorporation of many-body effects into an atomic quantum coherence theory can be accomplished straightforwardly using the screened Hartree–Fock approximation. The result is a more complete description of semiconductor behaviour, in particular the carrier density dependences of the energy levels and optical transition strengths, which can be combined with a realistic model of the QD electronic structure. To illustrate QD quantum-coherence effects including many-body contributions, the optical response to an optical drive pulse is calculated for InAs QDs and compared with the results for an independent-particle model. The influence of the Coulomb interaction (together with the QD energy spectrum) leads to different predictions concerning the spectral shape of the optical response and the achievable group-velocity slowdown. When many-body effects are neglected, one seriously overestimates the drive intensity requirement for quantum coherence to occur and obtains different predictions on the spectral regions where group-velocity slowdown and excitation-induced transparency (or amplification) coexist. The influence of different Coulomb renormalization contributions is also discussed. It is shown how a combination of transition energy and Rabi-energy renormalizations lead to the reduced pump-intensity requirements.

Acknowledgements

A grant for CPU time from the NIC at the Forschungszentrum Jülich is gratefully acknowledged. The work is also partially funded by the US Department of Energy under contract DE-AC04-94AL85000 and the Humboldt Foundation.

References

[1] S.E. Harris, J.E. Field and A. Imamoglu, Phys. Rev. Lett. **64** 1107 (1990).
[2] M.O. Scully, S.Y. Zhu and A. Gavrielides, Phys. Rev. Lett. **62** 2813 (1989).
[3] M. Fleischhauer, A. Imamoglu and J.P. Marangos, Rev. Mod. Phys. **77** 633 (2005).
[4] M. Phillips and H.L. Wang, Phys. Rev. Lett. **89** 186401 (2002).
[5] Z.S. Yang, N.H. Kwong, R. Binder, *et al.*, J. Opt. Soc. Am. B **22** 2144 (2005).
[6] S. Sarkar, P. Palinginis, P.C. Ku, *et al.*, Phys. Rev. B **72** 035343 (2005).
[7] S.W. Chang, S.L. Chuang, P.C. Ku, *et al.*, Phys. Rev. B **70** 235333 (2004).
[8] D.D. Smith, H. Chang, K.A. Fuller, *et al.*, Phys. Rev. A **69** 063804 (2004).
[9] D.E. Nikonov, A. Imamoglu and M.O. Scully, Phys. Rev. B **59** 12215 (1999).
[10] C.J. Chang-Hasnain, P.C. Ku, J. Kim, *et al.*, Proc. IEEE **91** 1884 (2003).
[11] W.W. Chow, H.C. Schneider and M.C. Phillips, Phys. Rev. A **68** 053802 (2003).
[12] P. Borri, W. Langbein, S. Schneider, *et al.*, Phys. Rev. Lett. **87** 157401 (2001).
[13] A.A. Belyanin, F. Capasso, V.V. Kocharovsky, *et al.*, Phys. Rev. A **63** 053803 (2001).
[14] S. Michael, W.W. Chow and H.C. Schneider, Appl. Phys. Lett. **89** 181114 (2006).
[15] *nextnano*^{3} device simulator, see http://www.wsi.tum.de/nextnano
[16] O. Stier, M. Grundmann and D. Bimberg, Phys. Rev. B **59** 5688 (1999).
[17] W.W. Chow and S.W. Koch, *Semiconductor-Laser Fundamentals* (Springer, Berlin, 1999).
[18] H.C. Schneider, W.W. Chow and S.W. Koch, Phys. Rev. B **64** 115315 (2001).
[19] H.C. Schneider, W.W. Chow and S.W. Koch, Phys. Rev. B **70** 235308 (2004).
[20] P. Borri, W. Langbein, S. Schneider, *et al.*, IEEE J. Sel. Top. Quantum Elect. **8** 984 (2002).
[21] L.V. Hau, S.E. Harris, Z. Dutton, *et al.*, Nature **397** 594 (1999).
[22] D.F. Phillips, A. Fleischhauer, A. Mair, *et al.*, Phys. Rev. Lett. **86** 783 (2001).
[23] M. Bajcsy, A.S. Zibrov and M.D. Lukin, Nature **426** 638 (2003).

Distribution

1	MS 0123	LDRD Office, 01011
1	MS1086	Weng Chow, 01123
1	MS1086	Dan Barton, 01123
1	MS1421	Jerry Simmons, 01130
1	MS1427	Julia Phillips, 01100
1	MS0899	Technical Library, 9536 (electronic copy)


Sandia National Laboratories